



HAL
open science

The Measured Relationship between Ice Water Content and Cloud Radar Reflectivity in Tropical Convective clouds.

Alain Protat, Julien Delanoë, J. W. Strapp, E. Fontaine, D. Leroy, Alfons Schwarzenboeck, L. Lilie, C. Davison, F. Dezitter, A. Grandin, et al.

► **To cite this version:**

Alain Protat, Julien Delanoë, J. W. Strapp, E. Fontaine, D. Leroy, et al.. The Measured Relationship between Ice Water Content and Cloud Radar Reflectivity in Tropical Convective clouds.. Journal of Applied Meteorology and Climatology, 2016, 55 (8), pp.1707-1729. 10.1175/JAMC-D-15-0248.1 . insu-01322886

HAL Id: insu-01322886

<https://insu.hal.science/insu-01322886>

Submitted on 9 Nov 2020

HAL is a multi-disciplinary open access archive for the deposit and dissemination of scientific research documents, whether they are published or not. The documents may come from teaching and research institutions in France or abroad, or from public or private research centers.

L'archive ouverte pluridisciplinaire **HAL**, est destinée au dépôt et à la diffusion de documents scientifiques de niveau recherche, publiés ou non, émanant des établissements d'enseignement et de recherche français ou étrangers, des laboratoires publics ou privés.

The Measured Relationship between Ice Water Content and Cloud Radar Reflectivity in Tropical Convective Clouds

A. PROTAT,^a J. DELANOË,^b J. W. STRAPP,^c E. FONTAINE,^d D. LEROY,^d A. SCHWARZENBOECK,^d
L. LILIE,^e C. DAVISON,^f F. DEZITTER,^g A. GRANDIN,^g AND M. WEBER^g

^a *Research and Development Branch, Australian Bureau of Meteorology, Melbourne, Victoria, Australia*

^b *Laboratoire des Atmosphère Milieux Observations Spatiales (LATMOS), Guyancourt, France*

^c *Met Analytics Inc., Toronto, Ontario, Canada*

^d *Laboratoire de Météorologie Physique (LaMP), Université Blaise Pascal, Clermont-Ferrand, France*

^e *Science Engineering Associates, Mansfield Center, Connecticut*

^f *National Research Council Canada, Ottawa, Ontario, Canada*

^g *Airbus, Inc., Toulouse, France*

(Manuscript received 14 September 2015, in final form 2 May 2016)

ABSTRACT

In this paper, unprecedented bulk measurements of ice water content (IWC) up to approximately 5 g m^{-3} and 95-GHz radar reflectivities Z_{95} are used to analyze the statistical relationship between these two quantities and its variability. The unique aspect of this study is that these IWC– Z_{95} relationships do not use assumptions on cloud microphysics or backscattering calculations. IWCs greater than 2 g m^{-3} are also included for the first time in such an analysis, owing to improved bulk IWC probe technology and a flight program targeting high ice water content. Using a single IWC– Z_{95} relationship allows for the retrieval of IWC from radar reflectivities with less than 30% bias and 40%–70% rms difference. These errors can be reduced further, down to 10%–20% bias over the whole IWC range, using the temperature variability of this relationship. IWC errors largely increase for $Z_{95} > 16 \text{ dBZ}$, as a result of the distortion of the IWC– Z_{95} relationship by non-Rayleigh scattering effects. A nonlinear relationship is proposed to reduce these errors down to 20% bias and 20%–35% rms differences. This nonlinear relationship also outperforms the temperature-dependent IWC– Z_{95} relationship for convective profiles. The joint frequency distribution of IWC and temperature within and around deep tropical convective cores shows that at the $-50^\circ \pm 5^\circ \text{C}$ level, the cruise altitude of many commercial jet aircraft, IWCs greater than 1.5 g m^{-3} were found exclusively in convective profiles.

1. Introduction

Cloud microphysical properties are major drivers of cloud–radiation interactions, through complex processes that are still a challenge to accurately simulate in large-scale models. The vertical distribution of ice water content (IWC) inside nonprecipitating and deep convective clouds plays a central role in the interaction between clouds and incoming and outgoing radiation (e.g., Stephens et al. 1990). Different climate models still produce a very different ice water path, spanning up to an order of magnitude difference (Waliser et al. 2009; Li et al.

2012). New global datasets (Delanoë and Hogan 2010; Deng et al. 2013) offer new avenues to shed more light on the global and regional properties of nonprecipitating ice cloud microphysics, the cloud–radiation interactions, and the relationship between cloud properties and the large-scale environment (e.g., Su et al. 2008; Protat et al. 2011).

Although the retrieval of IWC in nonprecipitating ice clouds has been found to be reasonably accurate (Mace 2010; Protat et al. 2010a; Deng et al. 2013; Delanoë et al. 2013; Avery et al. 2012), there are reasons to believe this is not the case for convective cloud systems. The *CloudSat* IWC retrieval techniques currently rely on an assumed single statistical relationship between 95-GHz radar reflectivity (denoted as Z_{95}) and IWC, sometimes with temperature T as an additional constraint (e.g., Hogan et al. 2006; Protat et al. 2007, hereinafter referred to as P07). These IWC– Z_{95} and IWC– Z_{95} – T

Corresponding author address: Alain Protat, Australian Bureau of Meteorology, 700 Collins St., Docklands, Melbourne, VIC 3008, Australia.

E-mail: a.protat@bom.gov.au

relationships were derived from aircraft in situ microphysical data collected in nonprecipitating ice clouds at midlatitude and tropical locations, and did not include any data collected within and around deep convective cores. Furthermore, these relationships were not derived using direct measurements of IWC and Z_{95} . Rather, IWC was generally estimated from measured particle size distributions (PSDs) and a prescribed single statistical relationship between ice crystal mass and diameter [the so-called $m(D)$ relationship], while Z_{95} was also simulated using the same PSD measurements and assumed $m(D)$ relationship as inputs into T-matrix (Mishchenko et al. 1996) or simpler non-Rayleigh scattering calculations for spherical particles with corrected densities (e.g., Hogan et al. 2006; P07). The resulting variability around the fitted IWC– Z_{95} relationship was found to be very large in these studies, with IWCs having up to an order of magnitude difference for a given Z_{95} , as discussed in, for example, Matrosov et al. (2002) and P07. An unknown fraction of this variability could actually be artificially produced by the use of a single $m(D)$ for all ice clouds. More recent studies have used either bulk IWC or Z_{95} measurements combined with PSD measurements in order to refine $m(D)$ (e.g., A. J. Heymsfield et al. 2010, hereinafter referred to as H10) or to include some of its variability in the calculations (e.g., Fontaine et al. 2014, hereinafter referred to as F14). However, in none of these studies were both bulk IWC and Z_{95} measurements available to directly characterize the real variability of the IWC– Z_{95} relationship.

It is also obvious in past studies that the fitted IWC– Z_{95} power-law relationship does not capture at all the largest IWCs simulated from the PSDs, owing to the non-Rayleigh scattering effects at 95 GHz distorting the IWC– Z_{95} relationship for high IWCs (see, e.g., the right panels in Fig. 1 in P07). This is why Matrosov and Heymsfield (2008, hereinafter referred to as MH08) developed a specific *CloudSat* IWC– Z_{95} relationship using only data points for which $Z_{95} > 0$ dBZ. However, this MH08 relationship is still based on IWCs and Z_{95} derived from measured PSDs and assumes a single $m(D)$ for all ice clouds. In addition, the maximum estimated IWC and Z_{95} values included in the MH08 study were 2 g m^{-3} and 14 dBZ, respectively. This relationship cannot be extrapolated to larger values.

High ice water content detrained by deep convection in the upper troposphere is also a significant issue for aviation safety, especially in the tropics and subtropics where jet engines are found to be susceptible to engine power loss and damage in the vicinity of deep convection (e.g., Lawson et al. 1998;

Mason et al. 2006; Grzych and Mason 2010; Strapp et al. 2016a), which have been related to a previously not well recognized form of engine icing involving high concentrations of small ice crystals, now referred to as ice crystal icing. Safety concerns related to these engines led the international regulation authorities and scientific community to organize an international airborne field campaign based in Darwin, Northern Territory, Australia, called the High Altitude Ice Crystal (HAIC)–High Ice Water Content (HIWC) campaign (Dezitter et al. 2013; Strapp et al. 2016a, see summary in section 2) during January–March 2014. Data collected during this field experiment include state-of-the-art particle size distribution, bulk IWC (including high values), and multibeam 95-GHz radar reflectivity measurements, providing an unprecedented opportunity to characterize the IWC– Z_{95} relationship and its true variability by using actual measurements.

The first objective of this paper is to develop and analyze the first ever IWC– Z_{95} relationship that does not include any assumption on the $m(D)$ relationship and that includes measured IWC values reaching about 5 g m^{-3} (section 3). We then investigate how accurately IWC can be characterized from Z_{95} alone or with additional inputs such as temperature and/or location within a convective cloud system (convective or stratiform region). Accordingly, the variability of the IWC– Z_{95} relationship as a function of temperature and as a function of a convective index is studied in section 4. These IWC– Z_{95} relationships are finally used in section 5 to derive a statistical representation of the vertical distribution of IWC in and around tropical deep convective cores. Further possible applications of these relationships are discussed in section 6.

2. The HAIC–HIWC Darwin campaign measurements

The HAIC–HIWC field campaign took place from 16 January to 7 March 2014 out of Darwin. Details of the field campaign can be found in Dezitter et al. (2013). Only information relevant to this study is given in this section. Large-scale active monsoon conditions resulting in intense convective activity over the northern part of Australia were well established throughout much of the duration of the campaign, allowing for 23 scientific flights (for a total of 72 flight hours) to be conducted in very favorable conditions. The flight strategy was developed in conjunction with an aviation industry working group and is contained in the High Ice Water Content Project Science Plan

(Strapp et al. 2016a). The objective was to fly a survey pattern through mesoscale convective system anvils at scales of approximately 200 km or larger, one that would initially include penetrations as close as possible to deep convective cores at flight altitude if deemed safe by the pilot. At least one convective core penetration and several flight legs in the immediate vicinity of the convective cores were ideally flown. In situ updrafts of up to 23 m s^{-1} were recorded at flight altitude, with peak updraft speeds exceeding 10 m s^{-1} in most flights. The maximum measured peak IWC was about 5 gm^{-3} , and water contents exceeding 2 gm^{-3} for over 60 nmi (111 km) were measured.

The aircraft platform used for this campaign was the French Service des Avions Français Instrumentés de Recherche en Environnement (SAFIRE) Falcon 20, equipped with a suite of in situ microphysics probes, bulk total water content (TWC) probes, and a 95-GHz Doppler cloud radar named Radar Aéroporté et Sol de Télédétection des Propriétés Nuageuses (RASTA; Protat et al. 2004; Protat et al. 2009; Delanoë et al. 2013). The endurance of the Falcon 20 is 3.5 h, its nominal true airspeed is 200 m s^{-1} , and its ceiling is at about -50°C in the tropical atmosphere near Darwin.

a. *In situ* microphysical measurements

The PSD was measured from 1- to $6400\text{-}\mu\text{m}$ diameter using the Cloud Droplet Probe (CDP, size range $1\text{--}50 \mu\text{m}$, resolution of $2 \mu\text{m}$) from Droplet Measurement Technologies (DMT), the 2D-Stereo Probe [2D-S, size range $10\text{--}1280 \mu\text{m}$, resolution of $10 \mu\text{m}$; Lawson et al. (2006)] from the Stratton Park Engineering Company (SPEC, Inc.), and the Particle Imaging Probe (PIP, size range $100\text{--}6400 \mu\text{m}$, resolution of $100 \mu\text{m}$) from DMT (Baumgardner et al. 2011). These probes were fitted with antishattering tips so as to reduce the shattering of large ice crystals onto the probe tips (e.g., Korolev and Isaac 2005). Remaining shattered particles were then removed by means of software, using the very small interarrival time of shattered particles (e.g., Field et al. 2006; Heymsfield 2007). Both approaches are indeed needed for an efficient mitigation of shattering (e.g., Jackson et al. 2014). In the present paper, we use composite 2D-S-PIP PSDs, which were derived using a simple weighting technique described in F14.

The reference bulk IWC measurement was obtained using a new isokinetic evaporator TWC probe (IKP) that was originally developed between 2007 and 2011 by the National Research Council of Canada (NRC), Environment Canada (EC, now known as Environment and Climate Change Canada), and

Science Engineering Associates (SEA). The device was designed to measure high-IWC conditions up to 10 gm^{-3} at 200 m s^{-1} true airspeed in summer tropical and subtropical atmospheric conditions from -10° to -50°C , with a designed accuracy of 20%. A downsized version of the probe (IKP2) was then developed for NASA and the FAA in 2013 by SEA and NRC specifically to fit within the operational constraints of the Falcon 20 for the Darwin-2014 HAIC-HIWC flight measurement program. The operating principles of the IKP have been described by Davison et al. (2009), and are the same for the IKP2. The performance of the IKP2 probe has been assessed in multiple wind tunnel tests at four different facilities, and was found to operate without saturation and within 15% for water contents up to 5 gm^{-3} and airspeeds up to 150 m s^{-1} . More details on this probe can be found in Strapp et al. (2016b) and Davison et al. (2016). Since the IKP2 measures the total water content, in real conditions liquid water and water vapor contributions should be subtracted to obtain IWC. Unfortunately, the hot-wire LWC sensor on the aircraft was unable to measure LWC below about 10% of the IWC in mixed-phase conditions, and LWC levels exceeding this value were very rare. Fortunately, the Goodrich ice detector could be used to detect the presence of liquid water. Two such regions in two very short flight segments were identified at -10°C , and these regions were excluded from the subsequent comparisons. The minimum detectable IWC of the IKP2 is determined by the noise level of the water vapor measurements of the IKP2 and background probes. This resulting noise level of the subtraction of the background humidity from the IKP2 humidity is a function of temperature: it is about 0.1 gm^{-3} at -10°C , dropping rapidly to about 0.005 gm^{-3} at -50°C . Since most data were gathered at temperatures colder than about -25°C , a minimum IWC of 0.05 gm^{-3} was chosen as the threshold to include in our analysis. The IKP2 dataset used in this study is at 1-s resolution and is the official final full dataset.

A second hot-wire bulk IWC probe, the so-called Robust probe developed by SEA for EC and the NRC, was integrated onto the CDP canister. The system provided reliable measurements at high altitude and high IWC during flight tests conducted by Airbus in 2010 and 2011 (Grandin et al. 2014). Based on results from previous hot-wire probes, it was known that the Robust probe's collection efficiency for ice crystals would be significantly lower than unity. In this paper, we only use the Robust probe measurements to establish that the two very different bulk TWC probes provide highly correlated IWC

measurements. Statistical comparisons using all Darwin 2014 HAIC–HIWC flights (not shown) reveal that these two TWC measurements of quite different operating principles track very closely (correlation coefficient = 0.96, standard deviation of the difference between the two probes ranging from 20% at $IWC = 1 \text{ g m}^{-3}$ and decreasing roughly linearly down to about 5% at $IWC = 4 \text{ g m}^{-3}$), and that the overall efficiency factor for the Robust probe is close to 0.45 in this HIWC environment.

b. Airborne cloud radar measurements

The RASTA 95-GHz airborne cloud radar (Protat et al. 2004, 2009; Delanoë et al. 2013) provides the radar reflectivities used in this study. The unique setup of this instrument includes the multibeam antenna system (three noncollinear antennas looking upward and three noncollinear antennas looking downward), allowing for the 3D wind to be retrieved below and above the aircraft flight altitude in a pseudovertical cross section during straight-line flight patterns. The RASTA radar has been carefully calibrated using accurate measurements of gains and losses through each radar component, remote fixed targets of known backscatter cross sections, and the Li et al. (2005) ocean surface backscatter technique (Bouniol et al. 2008). Quantitative comparisons with the *CloudSat* spaceborne radar (Protat et al. 2009) also showed that the two radar reflectivities agreed to within 1 dB, while the *CloudSat* radar reflectivities also agreed statistically within 0.4 dB with cloud radar data from five different ground-based sites. These results give confidence that the RASTA cloud radar is well calibrated, within 1 dB. Radar reflectivities in linear units from the nadir and zenith antennas nearest to the aircraft were linearly spatially interpolated, typically over 360 m (since the first nadir and zenith radar bins are at 180-m range), to produce a time series of Z_{95} at flight level, with a 1.2-s temporal resolution. Deriving the IWC– Z_{95} relationships from the nadir or zenith reflectivities instead of the interpolated ones did not result in any change in the coefficients of these relationships. It must be acknowledged that since the RASTA radar frequency (W band, around 95 GHz) is much higher than the frequency of the pilot radars on commercial aircraft (X band, around 10 GHz), the IWC– Z_{95} relationships derived in the present paper cannot be readily used to mitigate the HIWC threat in real time on commercial aircraft. More work will be done in the near future to derive the same relationships at X band and to evaluate the differences with the relationships from this paper, when data become available.

3. The IWC– Z_{95} relationship in deep tropical convective clouds

As explained in section 1, the dataset collected during the HAIC–HIWC campaign using the IKP2 probe and the RASTA cloud radar allows us the unprecedented opportunity to characterize the IWC– Z_{95} relationship without any assumption on the PSD or the ice crystal mass–size relationship and including high values of IWC up to 5 g m^{-3} . For the sake of comparison with earlier approaches for which direct IWC and/or Z_{95} measurements were not available, we have also estimated IWC and Z_{95} using the PSD measurements, the single mass–size relationship used in P07 (which is that from Brown and Francis 1995), and T-matrix calculations using the aspect ratios estimated from the projected aspect ratio measured by raw in situ probes. This will be referred to as the PSD approach in the following. The resulting joint distribution of IWC and Z_{95} using this technique is shown in Fig. 1, using a Z_{95} and an IWC bin of 1 dB and 0.05 g m^{-3} , respectively. Figure 2 shows the same joint distribution but derived from direct IKP2 IWC and RASTA Z_{95} measurements. For the sake of comparisons between Figs. 1 and 2, the mean IKP2 IWC in each Z_{95} bin is also given in both figures. The joint distributions are normalized for each reflectivity bin by the sum of all points in each IWC bin. In other words the sum of IWC frequencies is 1 for each reflectivity bin. Using such normalization allows for changes in the width of the IWC distribution for each Z_{95} bin to be readily observed.

Figure 2 shows that there is a very well-defined power-law relationship between IWC and Z_{95} , characterized by a narrow IWC distribution width for Z_{95} of less than 10 dBZ. For $Z_{95} > 10$ dBZ the IWC distribution becomes wider, indicating that the retrieval of IWC from radar reflectivity will be characterized by larger errors for larger IWCs. This increase in the variability of IWC as a function of Z_{95} is consistent with the fact that higher 95-GHz radar reflectivities are more sensitive to the variabilities in the shape and density of the ice particles as non-Rayleigh scattering effects increase. Despite these potential effects though, the relationship is still well defined. It must be noted that there are currently no data available to assess whether this relationship can be applied to other regions of the world. This regional variability will be investigated to some extent in the future by collecting more data in different large-scale environments conducive to deep convection.

Comparison between Figs. 1 and 2 highlights the impact of using a single mass–size relationship and

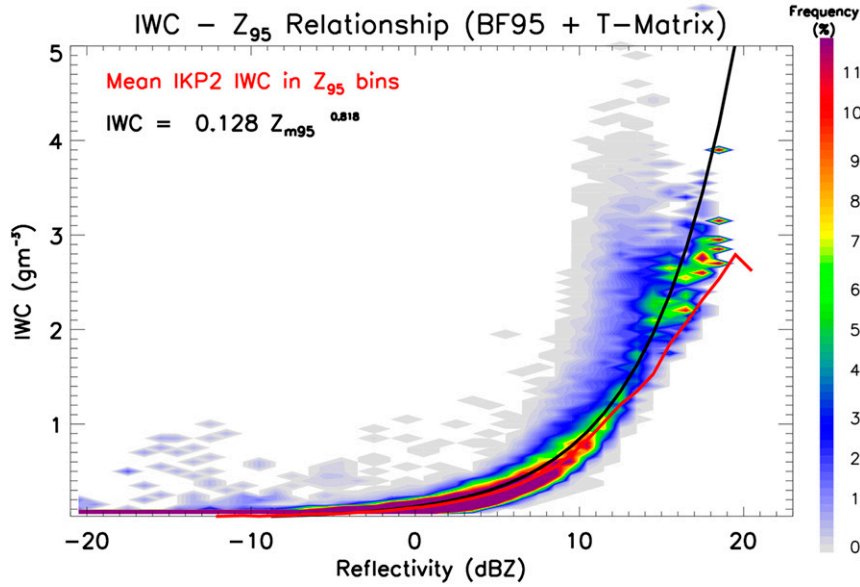


FIG. 1. Joint frequency distribution of simulated IWC and Z_{95} from all HAIC-HIWC flights, using Z_{95} and IWC bins of 1 dB and 0.05 g m^{-3} , respectively. Both IWC and Z_{95} are derived from the particle size distribution measurements and assuming the Brown and Francis (1995) mass-size relationship. The Z_{95} reflectivity is simulated using the T-matrix code. The frequencies are normalized by the total number of IWC points in each reflectivity bin. The solid black line is the power-law fit to the data. The red line is the mean IKP2 IWC in each Z_{95} bin.

T-matrix calculations versus direct measurements for the first time. For $Z_{95} < 5 \text{ dBZ}$, the widths of the IWC distribution are very similar for any Z_{95} bin. The differences between the two joint distributions are largest for $Z_{95} > 10 \text{ dBZ}$ and IWCs $> 1.5 \text{ g m}^{-3}$, where a bimodal distribution of Z_{95} as a function IWC appears with the PSD approach (Fig. 1; see the two possible values of Z_{95} for a given IWC for $\text{IWC} > 1.5 \text{ g m}^{-3}$). The more frequent of the two modes is in good agreement with the distribution obtained with the direct measurements (Fig. 2), with a tendency to slightly overestimate IWC for any Z_{95} . The second mode largely overestimates IWC. The IWC distribution is also generally wider when direct measurements are used. This result shows that the natural variability of the mass-size relationship tends to broaden the range of possible IWCs for any Z_{95} greater than 10 dBZ.

A simple power-law fit to the joint frequency distribution of Fig. 2 yields the following IWC- Z_{95} relationship:

$$\text{IWC} = 0.108 Z_{m95}^{0.770}, \quad (1)$$

where $Z_{m95} = 10^{Z_{95}/10.0}$ is the radar reflectivity expressed in linear units ($\text{mm}^6 \text{ m}^{-3}$). The solid red line in Fig. 2 shows the mean IKP2 IWC for each Z_{95} bin. The comparison of the power-law fit and the mean IWC values

shows that the power-law IWCs tend to slightly but systematically underestimate the mean IWC for $Z_{95} < 17 \text{ dBZ}$ and overestimate IWC for $Z_{95} > 17 \text{ dBZ}$. This is quantified further in Fig. 3 using the relative bias (hereinafter referred to as the bias) and the relative root-mean-square difference (hereinafter referred to as the rms difference) as a function of IWC and Z_{95} . Figure 3a shows that IWCs greater than 0.5 g m^{-3} can be retrieved from (1) with less than 30% bias and less than 40% rms difference. For IWCs lower than 0.5 g m^{-3} , the bias is less than 20% but the rms differences increase as IWC decreases, up to 70% for $\text{IWC} = 0.05 \text{ g m}^{-3}$. The cumulative frequency of the absolute errors (not shown) indicates that the absolute errors grow linearly as a function of IWC up to $\text{IWC} = 1.8 \text{ g m}^{-3}$, above which they tend to be constant at less than 0.5 g m^{-3} for 45% of the time and less than 1 g m^{-3} about 80% of the time.

It is also important to characterize the errors as a function of the reflectivity itself, since that is the way IWC is retrieved from (1). Figures 3c,d show that for $Z_{95} < 15 \text{ dBZ}$, there is a systematic underestimation of IWC by about 10%–20%, with rms differences decreasing linearly from 70% at $Z_{95} = 0 \text{ dBZ}$ to 30% for $Z_{95} = 15 \text{ dBZ}$. For $Z_{95} > 15 \text{ dBZ}$, the bias then sharply increases from -10% to about 50% between 15 and 21 dBZ, and the rms differences range from 30% to 55% in that reflectivity range. As observed in Fig. 2, these

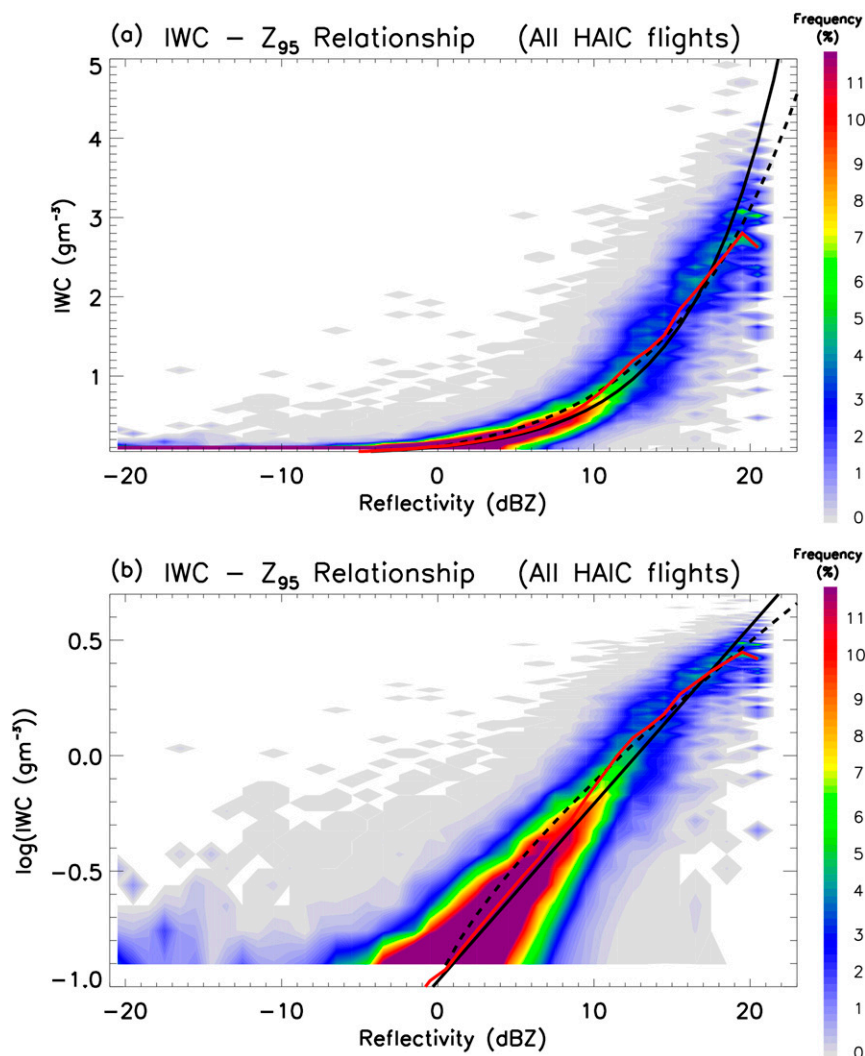


FIG. 2. Joint frequency distribution of measured IWC and Z_{95} from all HAIC-HIWC flights using Z_{95} and IWC bins of 1 dB and 0.05 g m^{-3} , respectively, on (a) linear and (b) logarithmic IWC scales. The frequencies are normalized by the total number of IWC points in each reflectivity bin. The solid black line is the power-law fit to the data [relationship (1); see text for details]. The dashed black line is a different fit [relationship (2); see text for details]. The solid red line is the mean IWC in each reflectivity bin. The total number of points is 83 231.

larger IWC errors for $Z_{95} > 17 \text{ dBZ}$ can be attributed to strong departures from the power-law shape in the joint IWC- Z_{95} distribution.

An important implication of this result is that although the errors are larger for $Z_{95} > 17 \text{ dBZ}$, non-Rayleigh scattering effects at the W band in that reflectivity range do not alter the accuracy of the IWC retrieval to a point that IWC cannot be retrieved. This indicates that ice crystals contributing to producing high IWC are not of a size large enough to induce large non-Rayleigh scattering effects. Matrosov and Heymsfield (2008) suggest that these errors can be reduced by using $Z_{95} > 0 \text{ dBZ}$ data only. Nevertheless, we found that the

power-law shape was still not suitable to reducing errors at high reflectivities. So we developed a nonlinear fit expressed as $\log(\text{IWC}) = aZ_{95}^b + c$ instead. The fit to the data yielded the following relationship:

$$\log(\text{IWC}) = 0.1564Z_{95}^{0.753} - 1.01, \quad (2)$$

with $Z_{95} > 0 \text{ dBZ}$.

This fit is shown in Fig. 2 (dashed line). The error analysis as a function of reflectivity (Fig. 4, dashed red) shows that IWCs retrieved using relationship (2) are slightly overestimated (bias less than 20% over the $[0; 10] \text{ dBZ}$ range) $Z_{95} < 10 \text{ dBZ}$, with a similar rms

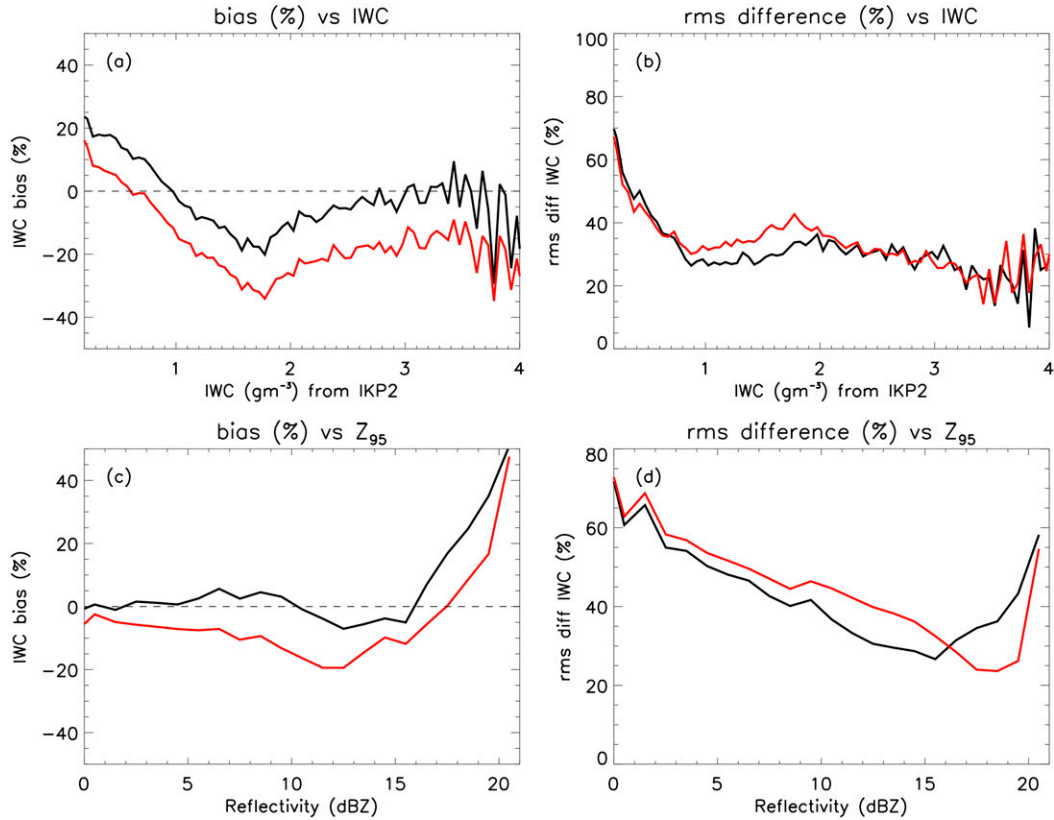


FIG. 3. Error analysis of radar-derived IWCs. The (a) bias and (b) rms difference as a function of the IKP2 IWC, and the (c) bias and (d) rms difference as a function of radar reflectivity, as derived from the IWC–Z₉₅–T (black) or IWC–Z₉₅ (red) relationship (1).

difference for the results from relationship (1). The main benefit, as expected, is in the large improvement in the IWC retrieval for Z₉₅ > 10 dBZ when compared to relationship (1) (cf. solid and dashed red lines in Fig. 4). The IWC retrieval bias is less than 10% up to Z₉₅ = 19 dBZ, and increases up to only 25% at Z₉₅ = 21 dBZ, which is a factor of 2 lower than when using relationship (1) (Fig. 4b). The rms difference decreases linearly from 65% to 20% between 0 and 20 dBZ, then

increases sharply and up to 35% at Z₉₅ = 21 dBZ (Fig. 4), which is again a large improvement over relationship (1), where the rms difference was up to 55% for Z₉₅ = 21 dBZ.

When using IWC–Z₉₅ relationships to retrieve IWC from Z₉₅, it is assumed implicitly that the radar calibration is perfect. As indicated above, we believe from our calibration work that the RASTA cloud radar calibration is accurate to within 1 dB. The effect of a

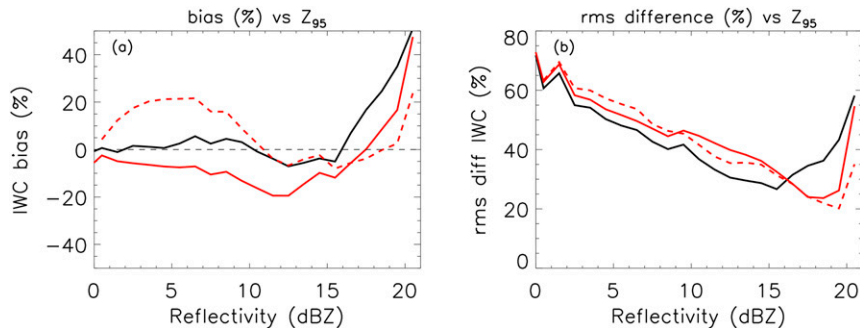


FIG. 4. Error analysis of radar-derived IWCs: (a) bias and (b) rms difference as a function of radar reflectivity, as derived from the IWC–Z₉₅–T relationship (black) and the IWC–Z₉₅ relationships (1) (red solid) and (2) (red dashed).

systematic 1-dB offset on the IWC retrieval can simply be estimated by fitting two power-law relationships such as (1) with 1 dB added or subtracted from the measured reflectivities, resulting in biases of +19% and -16%, respectively, over the whole reflectivity range. If the RASTA radar calibration is off by 1 dB, the IWCs produced using relationship (1) will be subject to this additional bias.

4. The variability of the IWC- Z_{95} relationship

In this section, we investigate two possible sources of the variability in the IWC- Z_{95} relationship shown in Fig. 2: the ambient temperature and the location within the convective cloud system (convective versus stratiform region). The underlying motivation for this variability study is to potentially use these parameters as additional constraints to the radar retrieval of IWC to reduce errors. It would have also been interesting to investigate the variability introduced by the underlying surface type (land versus ocean); however, too few cases of pure land-based convection were sampled during the HAIC-HIWC campaign. We also compare in this section the obtained relationships with tropical relationships found elsewhere in the literature.

a. Temperature variability

The IWC- Z_{95} relationships derived in Hogan et al. (2006) and P07 were found to vary with temperature. In contrast, MH08 did not report a large temperature variability in their dataset. Recently, F14 demonstrated using tropical anvil datasets that this variability could be very different for different $m(D)$ assumptions applied to the same PSD dataset, highlighting that previous studies may have overlooked this potential problem. Using their retrieved $m(D)$ and T-matrix calculations of radar reflectivity employing measured particle size distributions and ice crystal aspect ratios as inputs, F14 showed that errors in IWC could be reduced by 9%–12% with temperature-dependent IWC- Z_{95} relationships. However, there was no bulk IWC measurement to constrain the F14 datasets. Therefore, the HAIC-HIWC dataset again provides an unprecedented opportunity to directly measure (without any microphysical assumption) and analyze the variability of the IWC- Z_{95} relationship with temperature. The number of samples collected at each temperature level during the HAIC-HIWC experiment is given in Fig. 5f. This figure shows that over 1000 samples were collected at each temperature level from -50° to -10°C , and the largest number of samples was collected in the $[-45^\circ\text{C}; -35^\circ\text{C}]$ layer (over 12 000 samples). The variability of the joint IWC- Z_{95}

distribution with temperature is shown in the other panels of Fig. 5, where the HAIC-HIWC data between -55° and -5°C have been reorganized into 10°C bins. The following IWC- Z_{95} - T relationship was then derived from the whole HAIC-HIWC dataset:

$$\text{IWC} = 10^{a(T)Z_{95} + b(T)}, \quad (3)$$

$$a(T) = 1.173 \times 10^{-6} T^3 + 0.000109 T^2 + 0.003152 T + 0.1075, \quad \text{and} \quad (4)$$

$$b(T) = -1.071 \times 10^{-5} T^3 - 0.001112 T^2 - 0.04505 T - 1.606, \quad (5)$$

where T is the temperature ($^\circ\text{C}$). A third-order polynomial was required to adequately fit the $a(T)$ and $b(T)$ coefficients. Different possible functional forms of the $a(T)$ and $b(T)$ coefficients were tested, and those above provided the best error statistics. The IWC- Z_{95} - T relationships obtained by using (3)–(5) and the central temperature value of each temperature interval are shown in each panel of Fig. 5 (colored lines). The temperature variability of the IWC- Z_{95} relationship is found to be largest in the $0 \text{ dBZ} < Z_{95} < 13 \text{ dBZ}$ range, with IWC systematically larger for a given Z_{95} at lower temperatures in this reflectivity range. In contrast, for IWCs larger than about 2 g m^{-3} , Fig. 5 shows that the IWC- Z_{95} fit does a better or similar job at fitting the joint IWC- Z_{95} distribution, suggesting that temperature does not add any value for the retrieval of IWCs larger than 2 g m^{-3} . In general, as the temperature drops lower, the shape of the joint IWC- Z_{95} distribution departs more strongly from the power-law shape, especially in the $T = -50^\circ \pm 5^\circ\text{C}$ interval. Finally, we see that the joint distributions of IWC and Z_{95} are narrower in each temperature interval (Fig. 5) than when all temperatures are included (Fig. 2). This clearly indicates that a large part of the variability observed in Fig. 2 can indeed be attributed to temperature.

This large variability of the IWC- Z_{95} relationship with temperature suggests that the ratio of the number of large ice particles to medium/small ice particles changes with temperature, thereby changing the relationship between IWC (less sensitive to the large particles than Z_{95}) and Z_{95} (very sensitive to the size of the larger ice particles). This is investigated further in Fig. 6, which shows the mean PSD for all HAIC-HIWC flights in the same 10°C temperature intervals as in Fig. 5. The temperature variability of the PSD is characterized by two main signatures. Both signatures are consistent with small ice particle formation and growth through water vapor deposition processes dominating in the upper troposphere, followed by the aggregation process dominating during particle sedimentation at warmer temperatures in convective ice clouds (e.g.,

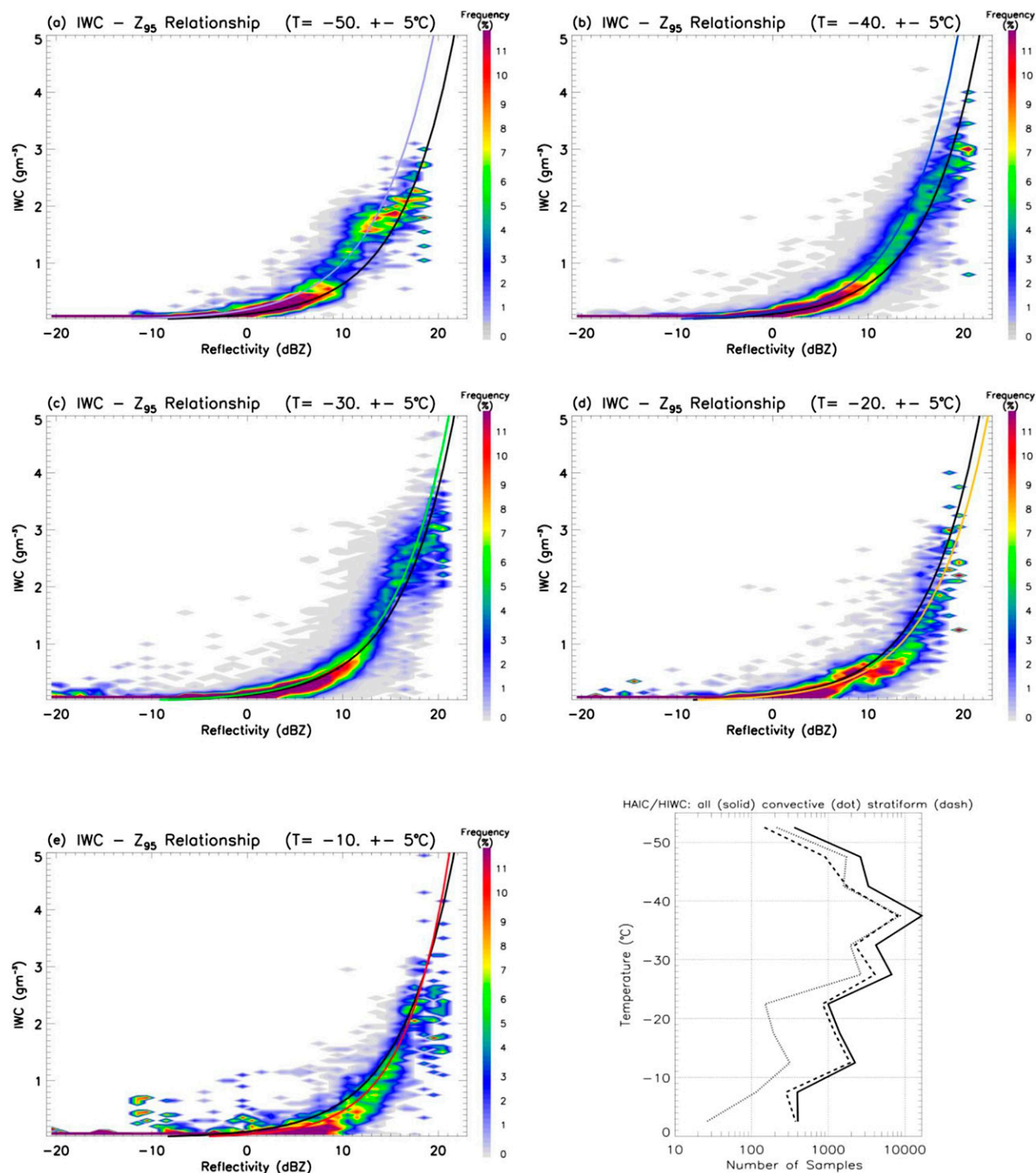


FIG. 5. As in Fig. 2, but for different temperature slabs: (a) $-50^\circ \pm 5^\circ\text{C}$, (b) $-40^\circ \pm 5^\circ\text{C}$, (c) $-30^\circ \pm 5^\circ\text{C}$, (d) $-20^\circ \pm 5^\circ\text{C}$, and (e) $-10^\circ \pm 5^\circ\text{C}$. The solid black line is the overall IWC-Z₉₅ fit, and the colored lines in each panel are the individual fits in each temperature slab. The solid red line is the mean IWC in each reflectivity bin. (f) The number of samples vs temperature using all profiles (solid), convective profiles (dotted), and stratiform profiles (dashed).

Protat et al. 2010b). The first signature is a strong increase in the number of large ice particles in the 2–8-mm maximum diameter range as temperature increases. The second signature is a decrease of similar magnitude in the

number of ice particles smaller than 1 mm, with the exception of the $-10^\circ \pm 5^\circ\text{C}$ temperature interval, where a very interesting increase in the number of particles smaller than 0.1 mm is observed, which may be an important result

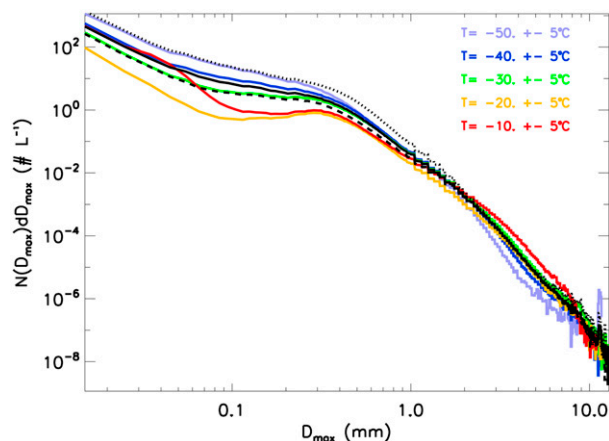


FIG. 6. Mean particle size distribution for all HAIC-HIWC flights (solid black), all convective profiles (dotted black), and all stratiform profiles (dashed black), as well as for the five temperature slabs in Fig. 5 using the same color code.

that can help us to understand the formation of high-IWC regions. This enhancement of the number of small particles may be the result of an efficient secondary ice production mechanism, such as that described by Hallett and Mossop (1974), where ice splinters are produced under certain conditions in a temperature window of -8° to -5°C . Ice crystal growth from supercooled liquid water lifted in ice phase by the convective updraft also potentially contributes to this increase in the number concentration of ice crystals of maximum diameter less than 0.1 mm. These processes will be investigated in more detail in a subsequent study, and are outside the scope of this paper. The main finding in Fig. 6 relevant to our understanding of the variability of the IWC- Z_{95} relationship with temperature is that the proportion of large to small particles increases with increasing temperature, implying lower IWCs for the same Z_{95} at warmer temperatures. This is fully consistent with the observed variability of the IWC- Z_{95} relationship with temperature in Fig. 5, as well as early studies (e.g., Heymsfield et al. 2013).

As observed in Fig. 7, where the IWC- Z_{95} - T relationship is superimposed every 10°C onto the initial overall joint distribution of Z_{95} and IWC, a large part of the variability in the joint frequency distribution is captured by the spread in the IWC- Z_{95} relationships for different temperatures. Figures 3a and 3b show that there is indeed a measurable improvement of about 15% in bias for IWC $> 1\text{ g m}^{-3}$ and a slight improvement of about 5% in the rms difference for $0.8\text{ g m}^{-3} < \text{IWC} < 2\text{ g m}^{-3}$ when using temperature as an additional constraint. Overall, Fig. 3 shows that IWC can be retrieved from (1) with a bias of less than 20% and an rms difference of less than 40% for IWC $> 0.5\text{ g m}^{-3}$.

The IWC errors as a function of reflectivity (Figs. 3c,d) show that there is indeed an improvement in the IWC bias when using temperature (biases are less than $\pm 5\%$), but only up to $Z_{95} = 16\text{ dBZ}$ (corresponding to a mean IKP2 IWC of about 2 g m^{-3}). For $Z_{95} > 16\text{ dBZ}$, the bias and rms difference get slightly larger when using temperature as an additional constraint. As discussed previously, this is due to non-Rayleigh scattering effects altering the relationship between IWC and Z_{95} at large Z_{95} . Figure 4 also indicates that relationship (2), derived using a nonlinear fit applied to data with $Z_{95} > 0\text{ dBZ}$, largely outperforms the IWC- Z_{95} - T relationship (3). This result shows that the temperature constraint is actually detrimental to the IWC retrieval for $Z_{95} > 16\text{ dBZ}$.

The added value of using temperature as an additional constraint depends on the temperature layer and the reflectivity value (Figs. 8–12). There is a clear difference in the errors for reflectivities lower and larger than about 15–16 dBZ, so we will describe the errors for the two reflectivity ranges $[0, 16]\text{ dBZ}$ and $[16, 21]\text{ dBZ}$ separately. As discussed previously, this is due to the growing impact of non-Rayleigh scattering on the shape of the IWC- Z_{95} relationship. We will first describe how the errors vary as a function of temperature for the IWC- Z_{95} relationship (1) and, then, analyze to what extent temperature helps reduce those errors.

For $Z_{95} < 15\text{--}16\text{ dBZ}$, relationship (1) produces negative IWC biases for low temperatures and positive biases for warmer temperatures. The IWC bias goes from -40% to -20% at $T = -50^{\circ} \pm 5^{\circ}\text{C}$ (Fig. 8) and to -20% at $T = -40^{\circ} \pm 5^{\circ}\text{C}$ (Fig. 9); it then reaches an overall minimum of $\pm 10\%$ at $T = -30^{\circ} \pm 5^{\circ}\text{C}$ (Fig. 10), before increasing to peak overestimations of 20%–40% for $T = -20^{\circ} \pm 5^{\circ}\text{C}$ in the $[0, 5]\text{ dBZ}$ and $[10, 15]\text{ dBZ}$ reflectivity intervals. The IWC bias is then largest at $T = -10^{\circ} \pm 5^{\circ}\text{C}$, reaching peaks of 60%–80% for $Z_{95} < 9\text{ dBZ}$. When using the nonlinear fit (2) between $\log(\text{IWC})$ and Z_{95} , which was designed to produce a better retrieval for large IWC (dashed red curves in Figs. 8–12), the IWC bias and rms difference at $Z_{95} < 15\text{--}16\text{ dBZ}$ are degraded when compared with results obtained with relationship (1), except for low temperatures, where some improvement is observed (Figs. 8 and 9). In contrast, when using temperature as an additional constraint for $Z_{95} < 15\text{--}16\text{ dBZ}$ (black curves in Figs. 8–12), the IWC bias remains small ($< 20\%$) at all temperature intervals, and much smaller than when using the IWC- Z_{95} relationship, except for the temperature interval $T = -30^{\circ} \pm 5^{\circ}\text{C}$, where temperature does not have much impact. In terms of rms differences, Figs. 8–12 show that there is a general improvement of about 5% in all individual temperature bins for $Z_{95} < 15\text{--}16\text{ dBZ}$.

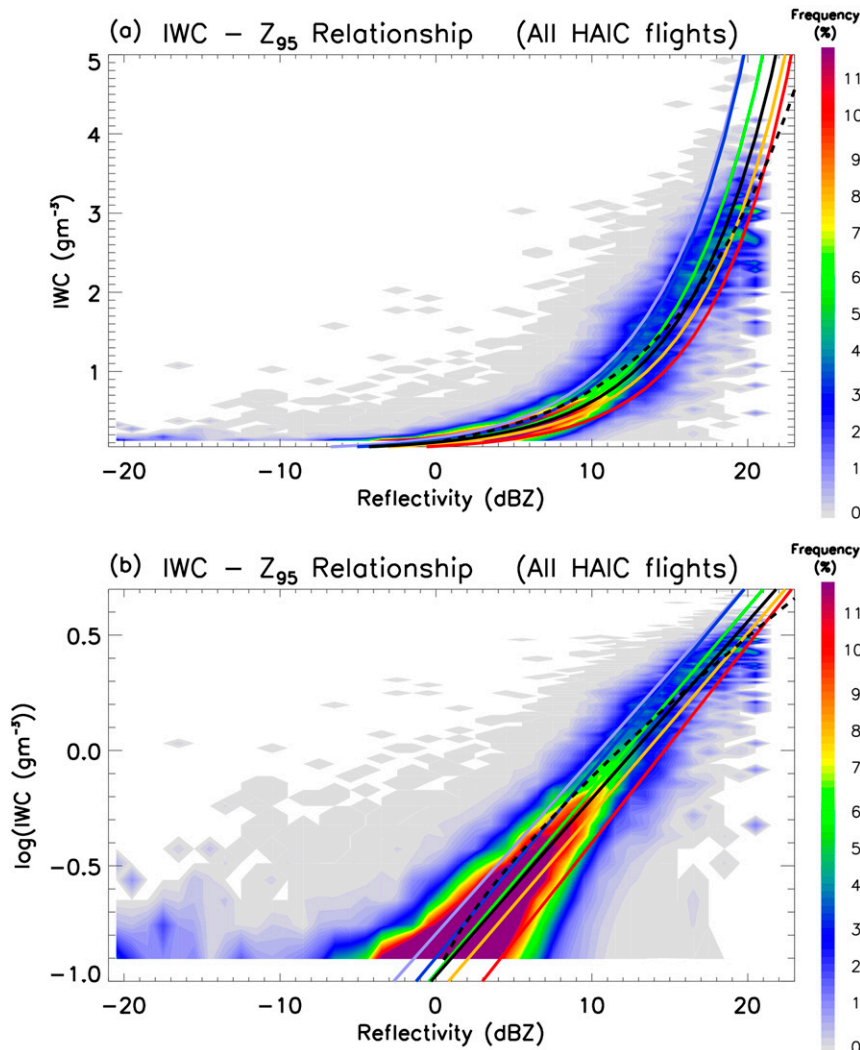


FIG. 7. As in Fig. 2, but with the different fits from different temperature slabs superimposed (light blue, $-50^{\circ} \pm 5^{\circ}\text{C}$; blue, $-40^{\circ} \pm 5^{\circ}\text{C}$; green, $-30^{\circ} \pm 5^{\circ}\text{C}$; orange, $-20^{\circ} \pm 5^{\circ}\text{C}$; and red, $-10^{\circ} \pm 5^{\circ}\text{C}$).

Figure 4 showed that the use of temperature as an additional constraint was overall slightly detrimental to the IWC retrieval for $Z_{95} > 16$ dBZ. Figures 8–12 further indicate that there is a compensating effect between the largely detrimental effects at low temperatures and the added value at warmer temperatures. The detrimental effect for $Z_{95} > 16$ dBZ is indeed only found at lower temperatures [especially $T = -50^{\circ} \pm 5^{\circ}\text{C}$ (Fig. 8) and $T = -40^{\circ} \pm 5^{\circ}\text{C}$ (Fig. 9)]. In these two temperature bins, it is therefore recommended to use IWC– Z_{95} relationships (1) or (2), not the temperature-dependent relationship (3). Using temperature has very little impact on the IWC retrieval at $T = -30^{\circ} \pm 5^{\circ}\text{C}$, while at warmer temperatures ($T = -20^{\circ} \pm 5^{\circ}\text{C}$ and $T = -10^{\circ} \pm 5^{\circ}\text{C}$), the use of temperature does improve the IWC bias and rms difference. Relationship (3) even performs at

the same level or slightly better than the nonlinear relationship (2), which was designed for better high IWC retrieval.

In conclusion the addition of the temperature constraint in the IWC– Z_{95} – T relationship (3) is overall largely beneficial, except when Z_{95} is larger than 16 dBZ for temperatures lower than -25°C . It is advised to use the nonlinear relationship (2) between $\log(\text{IWC})$ and Z_{95} in that case.

b. Convective–stratiform variability

Convective and stratiform regions of tropical deep convective cloud storms are known to be characterized by different drop size distributions [e.g., Bringi et al. (2009), Thurai et al. (2010), and Penide et al. (2013a) for the Darwin region] and ice particle size distributions

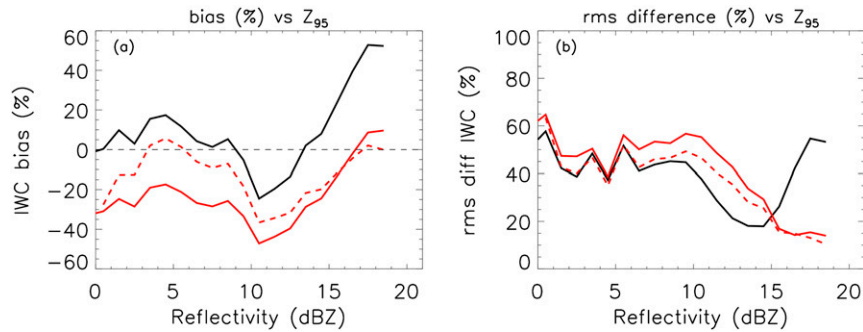


FIG. 8. As in Fig. 4, but for the $-50^{\circ} \pm 5^{\circ}\text{C}$ temperature slab.

(Heymsfield et al. 2013). These convective and stratiform regions can be classified with ground-based weather radars using indices derived from reflectivity [magnitude, texture, presence of so-called radar bright band below the 0°C isotherm altitude; e.g., Steiner et al. (1995)] or from the retrieval of the drop size distribution parameters if the radar has dual-polarization capabilities (e.g., Thurai et al. 2010; Penide et al. 2013b). It is therefore of interest to investigate whether some of the variability of the IWC– Z_{95} relationship is due to microphysical differences between convective and stratiform regions. Overall, the convective region is characterized by updrafts and downdrafts routinely exceeding $5\text{--}10\text{ m s}^{-1}$ above the melting layer in tropical convective cores (e.g., May and Rajopadhyaya 1999; May et al. 2002; G. M. Heymsfield et al. 2010; Giangrande et al. 2013) while the stratiform region is characterized by a slight updraft in ice phase and slight downdraft in liquid phase, generally not exceeding a few tens of centimeters per second [e.g., Protat and Williams (2011) for the Darwin region; Gamache and Houze 1982; Chong et al. 1987; Nishi et al. 2007]. To separate the RASTA cloud radar profiles into convective and stratiform profiles, we have developed a simple convective index based on the maximum of the drafts. The RASTA cloud radar multibeam measurements allow for the vertical profile of the two horizontal wind components

and the sum of the vertical velocity w and reflectivity-weighted terminal velocity V_T to be retrieved using the three noncollinear Doppler velocity measurements as inputs into a multi-Doppler ground-based radar retrieval technique adapted to the airborne configuration [technique described in Protat and Zawadzki (1999); Collis et al. (2013)]. The criterion we use is that if $(V_T + w)$ is greater than 1 m s^{-1} or smaller than -3 m s^{-1} for at least 1 km in height above the 0°C isotherm altitude (i.e., in ice phase), then the cloud radar profile is classified as convective. Otherwise, it is classified as stratiform.

Joint frequency distributions of Z_{95} and IWC derived using the convective and stratiform profiles from all HAIC–HIWC flights are shown in Figs. 13a and 13b, respectively. Again, power-law relationships are also fitted to the joint frequency distributions to produce IWC– Z_{95} relationships:

$$\text{convective IWC} = 0.152Z_{m95}^{0.715} \quad \text{and} \quad (6)$$

$$\text{stratiform IWC} = 0.103Z_{m95}^{0.749}. \quad (7)$$

From Fig. 13, it is clearly observed that for any given Z_{95} , IWC is systematically larger for convective profiles than for stratiform profiles. For instance, for $Z_{95} = 20\text{ dBZ}$, the mean IWC is 4.1 g m^{-3} in convective profiles and 3.2 g m^{-3} in stratiform profiles ($\sim 25\%$ increase

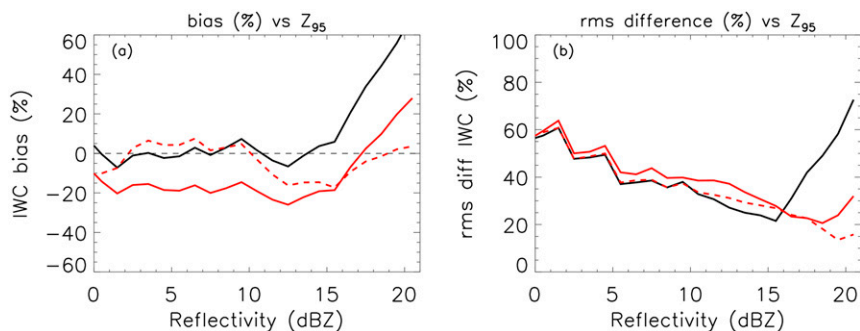


FIG. 9. As in Fig. 4, but for the $-40^{\circ} \pm 5^{\circ}\text{C}$ temperature slab.

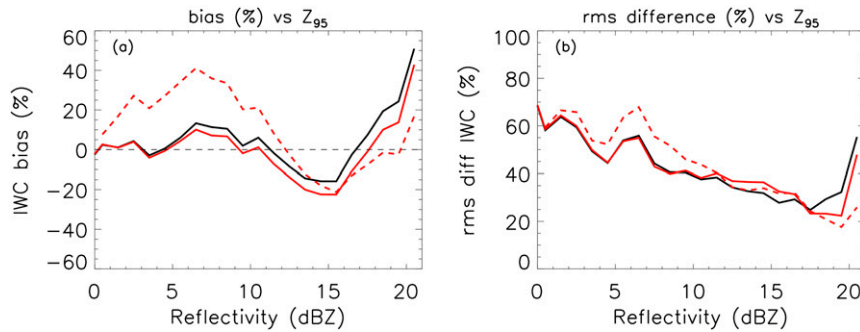


FIG. 10. As in Fig. 4, but for the $-30^{\circ} \pm 5^{\circ}\text{C}$ temperature slab.

in IWC). A much higher frequency of occurrence of $\text{IWC} > 2 \text{ g m}^{-3}$ is also found in the convective profiles. Differences between convective PSDs and stratiform PSDs (Fig. 6) provide further insights into the microphysical processes involved in the large differences observed between the two $\text{IWC}-Z_{95}$ relationships. Figure 6 shows that convective profiles are characterized by a much larger number of particles of maximum diameter up to about 2 mm than stratiform profiles (an order of magnitude difference for $D_{\text{max}} \sim 0.1 \text{ mm}$), while the number of large particles is similar. This is consistent with larger IWCs for a given Z_{95} in convective profiles. This large difference in the number of smaller particles in convective profiles suggests again that the production of small ice in convective updrafts through secondary ice formation–multiplication has the potential to generate areas of high IWC with moderate Z_{95} .

Error analysis of IWC derived from the convective $\text{IWC}-Z_{95}$ and $\text{IWC}-Z_{95}-T$ relationships (Fig. 14) shows that the bias and rms difference as a function of Z_{95} are very similar with or without temperature for $Z_{95} > 9 \text{ dBZ}$, and the IWC bias is larger when using temperature for $Z_{95} < 9 \text{ dBZ}$ (Figs. 14a,b). Figures 14a,b show that the nonlinear relationship (2) between $\log(\text{IWC})$ and Z_{95} produces the best error statistics overall, with IWC biases less than $\pm 20\%$ over the [2, 21] dBZ range, and rms differences decreasing from about 80% at $Z_{95} = 0 \text{ dBZ}$ down to 20%–30% for $Z_{95} > 15 \text{ dBZ}$.

Error analysis of IWC derived from the stratiform $\text{IWC}-Z_{95}$ relationship (7) (Fig. 15) shows that the use of temperature is beneficial to the IWC retrieval. Relationship (3) indeed outperforms relationships (1) and (2), with an IWC bias of less than $\pm 10\%$ over the whole reflectivity range and rms differences reduced by about 5%–10%, except for $Z_{95} > 16 \text{ dBZ}$, where relationships (1) and (2) slightly outperform the temperature-dependent relationship (3). Using relationship (3), the rms difference decreases linearly from 60% at $Z_{95} = 0 \text{ dBZ}$ to 30% at $Z_{95} = 15 \text{ dBZ}$, then, is of about 25%–35% for $Z_{95} > 15 \text{ dBZ}$.

Overall, this analysis shows that the nonlinear relationship (2) between $\log(\text{IWC})$ and Z_{95} should be used for convective profiles, and the temperature-dependent relationship (3) should be used for stratiform profiles. There is a large reduction of errors in stratiform IWC retrieval when temperature is used as a constraint, except for the bias in IWCs $< 0.8 \text{ g m}^{-3}$. The use of temperature yields improvement in bias by about 10% for IWCs $> 0.8 \text{ g m}^{-3}$ and in rms difference by about 30% for stratiform profiles over the whole IWC range.

c. Comparison with published $\text{IWC}-Z_{95}$ relationships

The $\text{IWC}-Z_{95}$ relationships from the HAIC–HIWC field experiment are for the first time derived from actual measurements of both IWC (including high values)

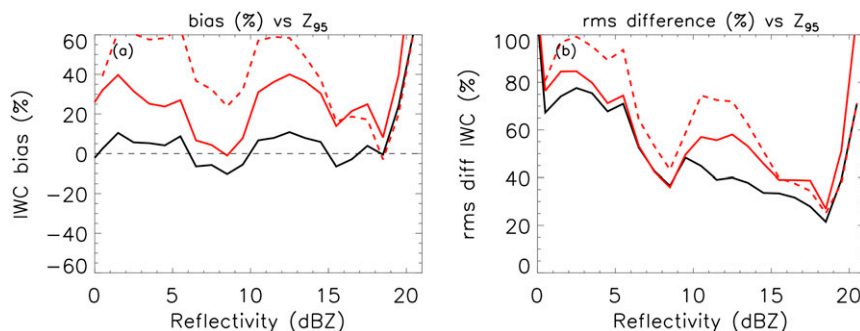


FIG. 11. As in Fig. 4, but for the $-20^{\circ} \pm 5^{\circ}\text{C}$ temperature slab.

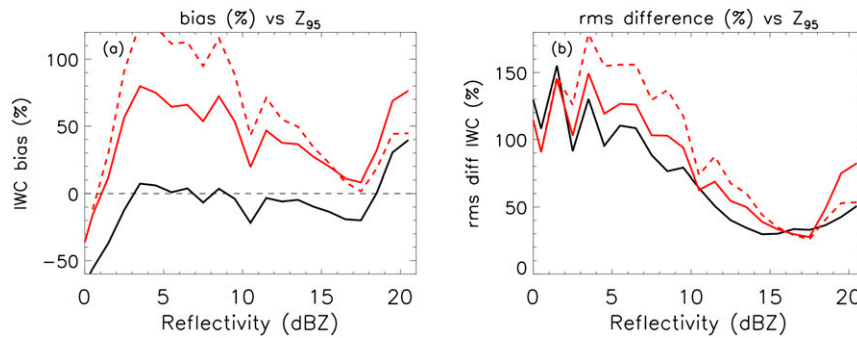


FIG. 12. As in Fig. 4, but for the $-10^{\circ} \pm 5^{\circ}\text{C}$ temperature slab.

and Z_{95} . It is therefore appropriate to compare these new relationships with those developed previously in the literature to assess their accuracy, as these earlier relationships have already been extensively used to derive IWC and build cloud climatologies from satellite measurements (e.g., Delanoë and Hogan 2010; Mace 2010; Deng et al. 2013), and to evaluate the representation of cloud microphysics in numerical weather prediction models (e.g., Illingworth et al. 2007; Bouniol et al. 2010; Delanoë et al. 2011). Below, we describe how these earlier tropical relationships were derived and compare them with the new HAIC–HIWC relationships.

The following relationships have been found in the tropical ice cloud literature: from Fontaine et al. (2014),

$$\text{IWC} = 0.098Z_{m95}^{0.805} \quad \text{and} \quad (8)$$

$$\text{IWC} = 0.087Z_{m95}^{0.775}; \quad (9)$$

from A. J. Heymsfield et al. (2010),

$$\text{IWC} = 0.110Z_{m95}^{0.662} \quad \text{and} \quad (10)$$

$$\text{IWC} = 0.240Z_{m95}^{0.664}; \quad (11)$$

from Matrosov and Heymsfield (2008),

$$\text{IWC} = 0.086Z_{m95}^{0.920}; \quad (12)$$

and, from Protat et al. (2007),

$$\text{IWC} = 0.149Z_{m95}^{0.681} \quad \text{and} \quad (13)$$

$$\text{IWC} = 0.198Z_{m95}^{0.701}. \quad (14)$$

Data used to derive the F14 relationships were collected almost exclusively in the stratiform region of deep tropical convective clouds over land [West Africa; (8)] and over the Indian Ocean [Maldives; (9)]. The same instrumentation and aircraft platform were used during these and the HAIC–HIWC campaigns, except that there was no bulk IWC measurement available for F14. The relationships

(8) and (9) were obtained by constraining the power-law $m(D)$ relationship with Z_{95} and in situ microphysical probe PSD measurements.

The H10 relationship (10) was obtained in convectively generated ice clouds during the Cirrus Regional Study of Tropical Anvils and Cirrus Layers–Florida–Area Cirrus Experiment (CRYSTAL-FACE; Jensen et al. 2004) and Tropical Composition, Cloud and Climate Coupling (TC4; Toon et al. 2010) tropical field experiments, which were carried out in Florida and Costa Rica, respectively. From these data a single $m(D)$ relationship was derived using PSD measurements and closure with bulk IWC measurements, and Z_{95} has been simulated from the PSD measurements using Mie calculations. Mostly tropical cirrus clouds generated by deep convection were measured during these experiments. Relationship (12) was also derived in MH08 from the CRYSTAL-FACE dataset and with the same technique as that presented in H10. However, only $Z_{95} > 0$ dBZ data were included in the IWC– Z_{95} power-law fit. Relationship (11) from H10 uses the same technique applied to the NASA African Monsoon Multidisciplinary Analyses (NAMMA; Zipser et al. 2009) dataset. Most data were collected in tropical stratiform clouds and in the vicinity of deep tropical convective cores off the coast of West Africa.

Finally the P07 relationships (13) and (14) were obtained from a very large dataset of PSD measurements compiled from several campaigns conducted in the midlatitudes and in the tropics. This dataset includes a large variety of ice clouds, from thin cirrus to stratiform ice. The Brown and Francis (1995) $m(D)$ relationship was assumed for all clouds. The quantity Z_{95} was calculated from the PSD measurements assuming spherical particles, but with a refractive index corrected following Oguchi (1983). Relationship (13) was obtained from the whole dataset, while relationship (14) was obtained using only the tropical data.

These relationships are all displayed in linear (Fig. 16a) and logarithmic (Fig. 16b) scales, together

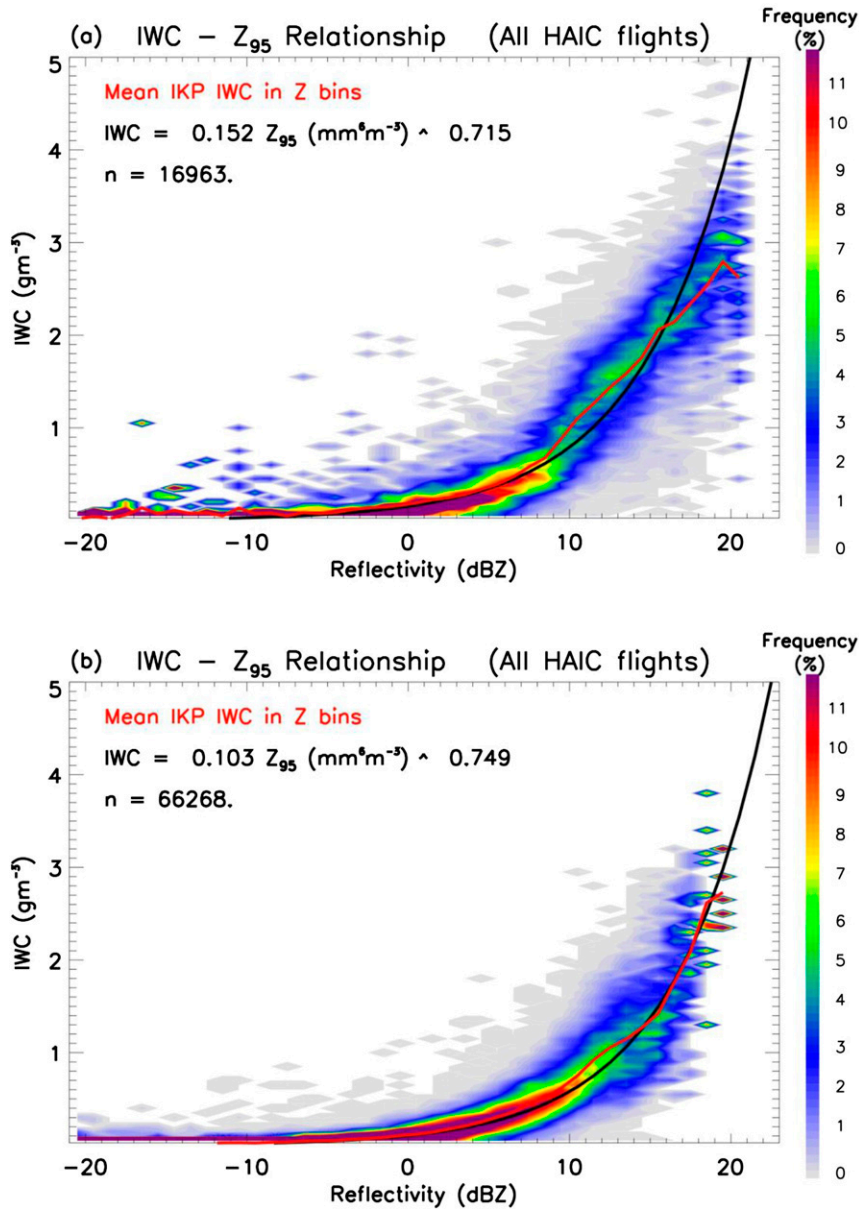


FIG. 13. As in Fig. 2a, but for (a) convective and (b) stratiform profiles.

with the HAIC–HIWC relationships: in (1) for all profiles, in (6) for convective profiles, and in (7) for stratiform profiles. Each relationship is drawn only within the IWC range that was used to derive them, either simulated from the PSDs or measured by a bulk IWC probe. Interestingly, the convective and stratiform relationships derived from the HAIC–HIWC dataset are bounded by the H10 relationships (10) and (11). For $Z_{95} > 10$ dBZ, the lowest IWCs are produced by relationship (10), which indicates that the IWCs in tropical cirrus are much lower for a given Z_{95} than IWCs closer to the convective cores. Using the equivalent-melted

diameter D_{eq} as the definition of the diameter of the ice crystals (e.g., Delanoë et al. 2005; Delanoë et al. 2014), Z_{95} is proportional to a higher moment of the PSD (sixth moment under the Rayleigh scattering approximation, slightly lower and variable in non-Rayleigh scattering situations) than IWC (third moment), where the n th moment of the PSD is defined as $M_n = \int N(D_{\text{eq}}) D_{\text{eq}}^n dD_{\text{eq}}$. In other words, IWC is less sensitive to size than Z_{95} . The observation of larger IWCs closer to the convective cores for a given Z_{95} therefore indicates that the total number of ice particles is much larger near convective cores than in stratiform regions and cirrus layers detrained farther

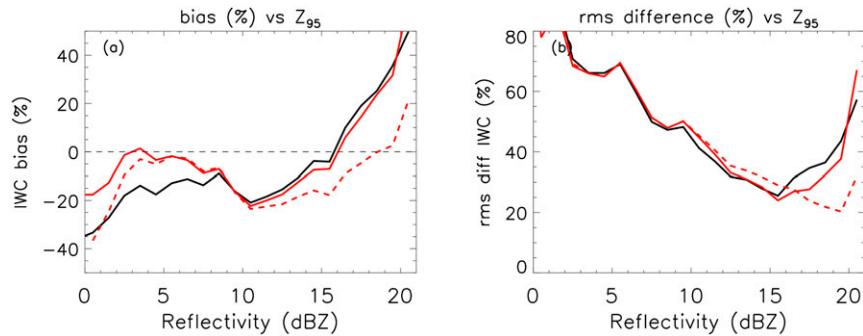


FIG. 14. As in Fig. 4, but for convective profiles.

away from these convective cores. This has been validated in Fig. 6 for convective and stratiform profiles; however, not enough samples were collected in the cirrus layers to include tropical cirrus results in the present study. This systematically higher total number of small ice particles close to the convective cores for a given Z_{95} is consistent with one of the main hypotheses put forth to explain the apparent lack of pilot awareness of impending ice crystal icing events, namely that a relatively small size of the ice crystals in a high-IWC environment would result in a low pilot X-band radar reflectivity that would be insufficient to warn of high-IWC conditions ahead, given the relatively high minimum threshold of a pilot radar (nominally 20 dBZ) (e.g., Mason et al. 2006).

It is also clearly observed in Fig. 16 that the F14 relationships (8) and (9) produce IWCs that are very similar to the general HAIC–HIWC relationship (1) and the stratiform HAIC–HIWC relationship (7), respectively. The F14 relationships were obtained in tropical stratiform anvils in two very different large-scale environments and over different underlying surfaces (end of the West African monsoon season over land vs weakly forced oceanic convection in the Indian Ocean). In practical terms, this result suggests that the variability of the IWC– Z_{95} relationship in tropical stratiform anvils as a function of the underlying surface

(land versus ocean) cannot be neglected and should be studied further. This is consistent with the reported morphological and microphysical differences of these stratiform regions along the tropical belt in Cetrone and Houze (2009).

In contrast, the P07 tropical relationship (14) is found to produce much larger IWCs than the HAIC–HIWC relationships, including the convective HAIC–HIWC relationship (6), although the dataset used in P07 does not include any measurement in convective clouds. This result suggests that the P07 relationship (14) likely overestimates IWC. This may be related to the use of the Brown and Francis (1995) $m(D)$ relationship, which was later found to overestimate the mass of ice crystals and to fail to capture dependences on temperature and particle size that are a result of the complex ice microphysical processes (H10). In contrast, the P07 relationship (13) obtained using the whole dataset including midlatitude stratiform ice clouds produces IWCs closer to the general HAIC–HIWC relationship (1) for $Z_{95} > 10$ dBZ, but produces much larger IWCs for $Z_{95} < 10$ dBZ [similar to the HAIC–HIWC convective relationship (6)]. This overestimation is also probably due to the choice of the Brown and Francis (1995) $m(D)$ relationship.

The only dataset other than HAIC–HIWC that includes data close to the convective cores is the NAMMA

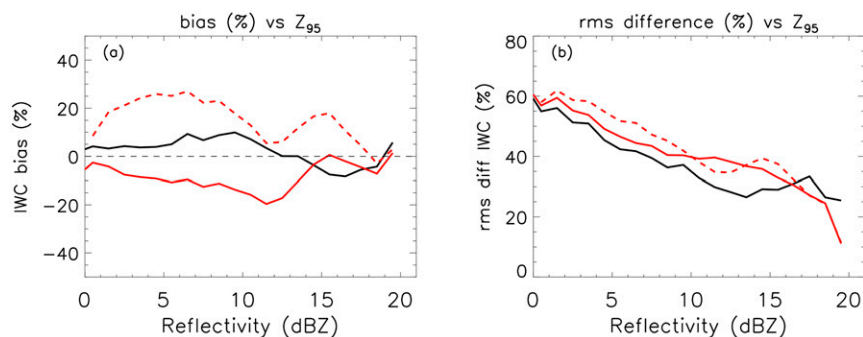


FIG. 15. As in Fig. 14, but for stratiform profiles.

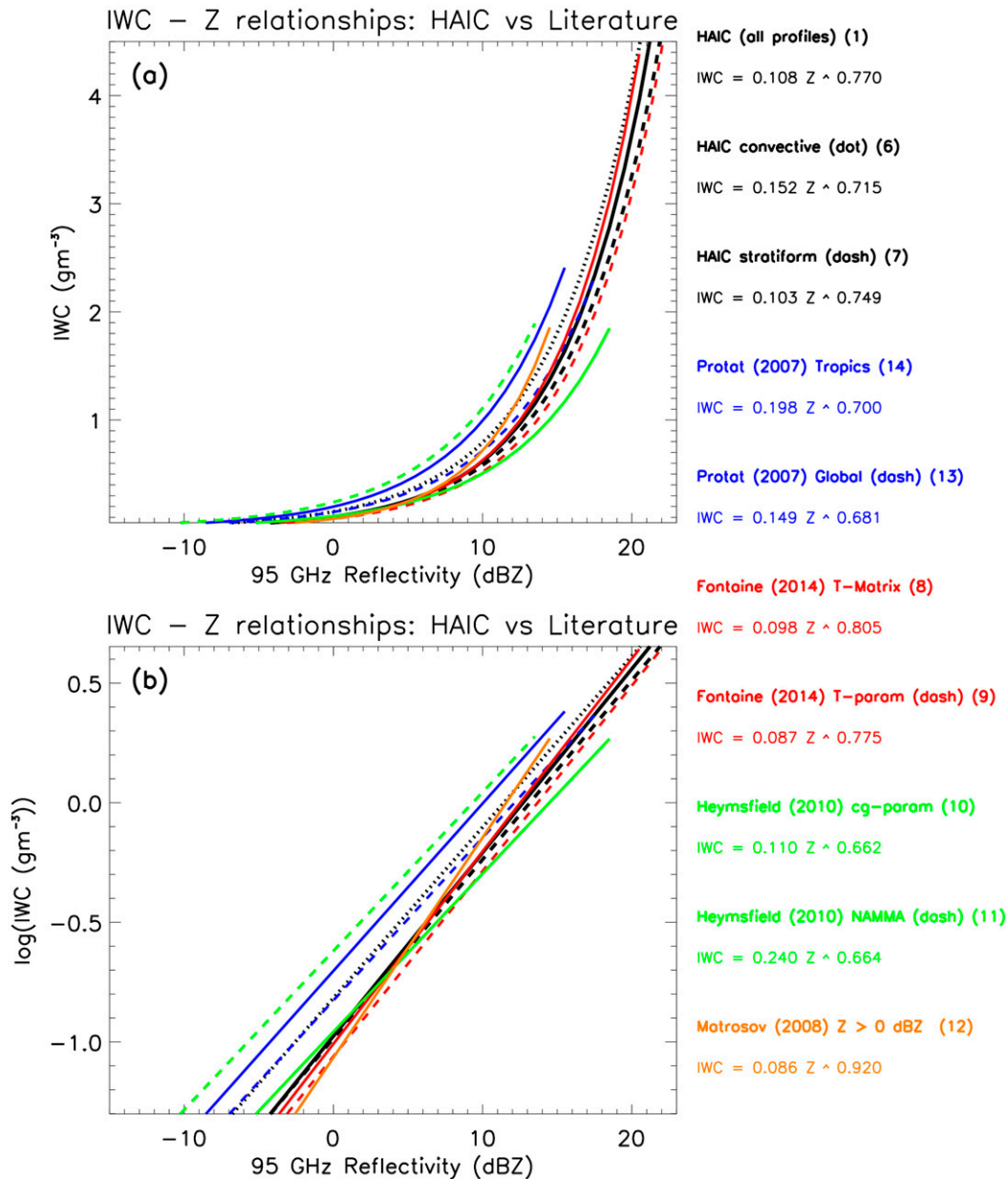


FIG. 16. Comparison between the HAIC–HIWC relationships and selected relationships from the literature in the tropics on (a) linear and (b) logarithmic scales. See text for details.

dataset, although the maximum values reported in this experiment did not exceed 2 gm^{-3} , possibly because of instrumental limitations. The IWC– Z_{95} relationship (11) derived from the NAMMA dataset appears to produce IWCs larger than the convective HAIC–HIWC relationship (6) in this IWC range.

MH08 only included reflectivities larger than 0 dBZ in an attempt to mitigate the departures from the power-law shape of the IWC– Z_{95} relationship when fitting a power law using the whole IWC range. As

observed in Fig. 16, the MH08 relationship tends to produce lower IWCs than the general [(1)] and convective [(6)] HAIC–HIWC relationships for $Z_{95} < 6 \text{ dBZ}$ and $Z_{95} < 12 \text{ dBZ}$, and produces consistent results with the HAIC–HIWC convective relationship (6) between 1 and 2 gm^{-3} . However, the MH08 study does not include any IWC values larger than 2 gm^{-3} . Extrapolating the MH08 relationship above 2 gm^{-3} is not recommended, as it would result in large overestimations of high IWCs. It is a major added

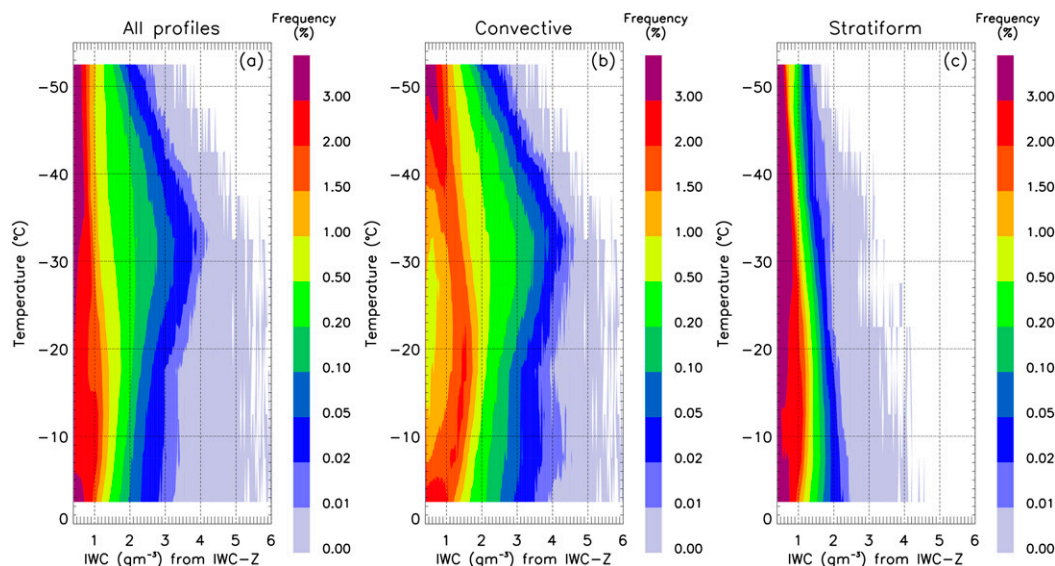


FIG. 17. Joint radar-derived IWC– T distribution for (a) all profiles, (b) convective profiles, and (c) stratiform profiles from the HAIC–HIWC field experiment. Probability distributions are normalized in such a way that frequencies sum to 1 in each temperature slab.

value of the HAIC–HIWC relationships that they are constrained with measured bulk IWC values exceeding 2 g m^{-3} .

5. The vertical distribution of IWC within and around tropical convective cores

One of the primary objectives of the HAIC–HIWC campaign is to characterize the microphysical properties of regions of high IWC produced by deep convective systems and the processes responsible for the formation and maintenance of these regions (Strapp et al. 2016a). Quantitative information about the 99th percentile of the IWC as a function of the distance scale will also be derived from the IKP2 reference IWC measurements at flight altitude in coming studies in order to validate a new ice crystal regulatory envelope (Government Printing Office 2010, appendix D; EASA 2011, appendix P) that has recently become law. The radar-derived IWC dataset has the potential to greatly expand the in situ TWC dataset collected by the IKP2 and therefore the amount of data possibly available for the assessment of the regulatory ice crystal envelope. Although the radar dataset has been demonstrated to contain increased uncertainty relative to in situ measurements, it is hoped that the much larger combined radar–in situ dataset may help reduce the statistical uncertainty of the results from an in situ–only analysis, as well as filling in additional altitudes that have been undersampled by in situ measurements as a result of practical limitations. Below, we examine some preliminary results of remotely detected

IWCs from the RASTA radar as a demonstration of how such results could be used to augment in situ measurements after a careful analysis of the data suitability.

Vertical profiles of radar-derived IWCs at $\sim 200\text{-m}$ scale from the HAIC–HIWC dataset matched with ambient temperatures from the European Centre for Medium-Range Weather Forecasts (ECMWF) reanalyses were assembled to characterize for the first time the vertical distribution (or temperature dependence) of high IWC in deep tropical convective clouds. Unlike the reference IKP2 probe, the RASTA airborne cloud radar measured radar reflectivity above and below the aircraft at 60-m vertical resolution, which allows for a first analysis of the vertical distribution of IWC in a high-IWC environment in our dataset over the whole troposphere. It must be noted that RASTA reflectivities are not corrected for attenuation to produce Fig. 17. Underestimations of IWC are therefore expected for vertical profiles that include graupel, in which W-band attenuation is expected to be large. However, graupel produce high X-band pilot radar reflectivity (30 dBZ or more), which does not correspond to HIWC conditions thought to cause engine events (e.g., Mason et al. 2006; Strapp et al. 2016a).

Errors associated with the use of ECMWF temperatures have also been estimated by comparing flight-level temperature measurements. The bias is 0.20°C and the rms difference is 0.74°C . When examining only the convective profiles (stratiform profiles), the bias and rms differences are 0.27° and 0.77°C (0.19° and 0.74°C), respectively. In light of these results, in order to estimate

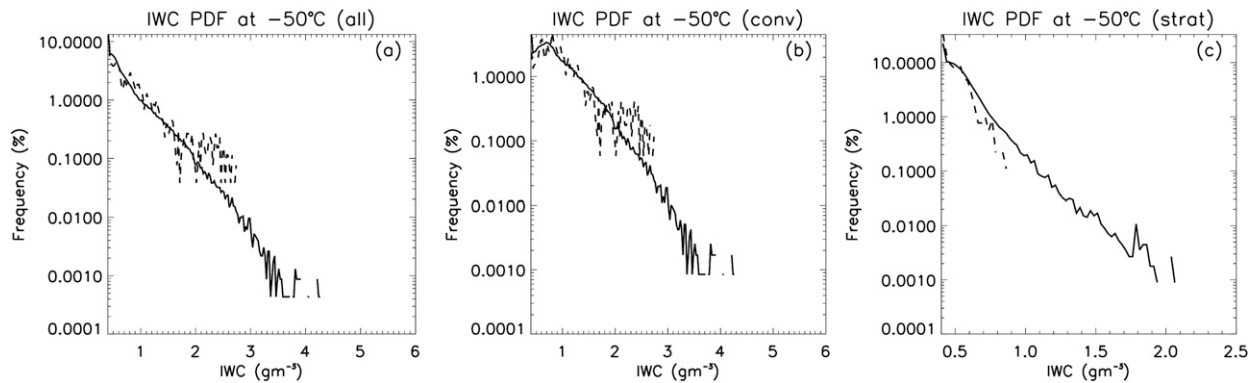


FIG. 18. PDFs of IWC derived from the whole radar vertical profiles (solid) and from the radar retrievals for flight level $-50^{\circ} \pm 5^{\circ}\text{C}$ (dashed) when (a) all profiles, (b) only convective profiles, or (c) only stratiform profiles are included.

the maximum IWC error due to temperature errors when using the $\text{IWC}-Z_{95}-T$ relationship, we have considered a maximum 1°C systematic overestimation, applied our relationship every 5°C in the interval from -10° to -50°C with or without the overestimation, and picked the maximum error produced. The maximum IWC error was less than 3% over the $[-10, 20]$ dBZ range. In other words, the ECMWF temperature errors translate into negligible errors on the IWC retrieval using the proposed $\text{IWC}-Z_{95}-T$ relationship.

The statistical distribution of radar-derived IWC as a function of temperature is shown in Fig. 17a. The results indicate that the probability of encountering large values of IWC increases with decreasing temperature up to -35°C . At -35°C , an IWC value of 4 g m^{-3} was found in 1% of the samples. This frequency of occurrence then quickly dropped for temperatures colder than -35°C . Values of IWC exceeding 4 g m^{-3} (5 g m^{-3}) were not detected at all at temperatures of -50°C (-35°C) or colder in our radar dataset, which suggests that these values may be rare. Separating these probabilities for convective and stratiform profiles (Fig. 17) using the convective–stratiform separation technique described in section 3b, IWC values greater than 4 g m^{-3} were exclusively found in convective profiles at all temperatures. IWC values greater than 3 g m^{-3} were also almost exclusively found in convective profiles and at temperatures colder than -25°C . Interestingly, an enhanced frequency of high IWC at the level from -10° to -5°C is also found in these convective profiles (Fig. 17b). This -10°C level is known to be important for microphysical growth processes, including ice particle growth from supercooled liquid water in convective updrafts and potentially ice multiplication–splintering through the Hallett–Mossop process (Hallett and Mossop 1974) and other secondary ice formation mechanisms. As discussed previously, PSDs in the -10°C layer are clearly

characterized by a large increase in the number of ice crystals smaller than 0.1 mm (Fig. 6), which is consistent with secondary ice production in that specific layer.

The highest priority temperature interval for the aviation regulatory interests is the $-50^{\circ} \pm 5^{\circ}\text{C}$ interval (Strapp et al. 2016a), as it corresponds to the typical cruise altitude for many commercial aircraft. At the -50°C level our radar IWC statistics indicate that values greater than approximately 1.5 g m^{-3} were only found in convective profiles (according to the radar retrievals) during the Darwin 2014 HAIC–HIWC experiment. Practically, this important result suggests that future research should focus on developing convective–stratiform indices from geostationary satellites to detect high IWC and mitigate the high-IWC threat to civil aviation at this flight level.

The IWC statistics of the $-50^{\circ} \pm 5^{\circ}\text{C}$ temperature interval derived from the entirety of the radar-derived IWC profiles are next compared to radar-derived IWCs at flight level from only the $-50^{\circ} \pm 5^{\circ}\text{C}$ temperature interval flight segments, using the same $\text{IWC}-Z_{95}$ relationship. Assuming that there is no bias in the nature of the flight segments executed at the other levels relative to those at -50°C (i.e., the clouds and cloud regions sampled at other altitudes are similar to those comprising the -50°C in situ dataset), and that there are no unidentified range-dependent errors in the radar IWC estimates, the differences in IWC PDFs are most likely due simply to the number of samples. Figure 18 shows the PDFs of IWC as a function of temperature for this temperature interval. The solid lines in Fig. 18 are the PDFs derived from the whole vertical profiles of IWC, and the dashed lines are the PDFs derived from the radar-derived IWCs at flight altitude. The flight-level PDFs are found to match the reference PDFs well down to the 0.1% frequency level, with a slight overestimation of the frequency of occurrence of IWCs of $2\text{--}3\text{ g m}^{-3}$ in

the convective profiles, along with an underestimation of the frequency of IWCs larger than 0.7 g m^{-3} in the stratiform profiles. Figure 18a–c also show that the PDFs at flight level are truncated at frequencies lower than about 0.1%. Since the regulatory objective is to derive 99th percentile values of IWC, this example analysis would suggest that the HAIC–HIWC in situ dataset should be sufficient to achieve this goal.

6. Conclusions

Unprecedented bulk measurements of ice water content up to about 5 g m^{-3} collocated with 95-GHz radar reflectivities were used in this study to analyze the IWC– Z_{95} relationship and its variability as a function of temperature and the nature of convection (convective vs stratiform). The unique aspect of this work is that, unlike past studies, these relationships do not include any assumptions about the statistical relationship between crystal mass and maximum dimension or any errors arising from scattering calculations of Z_{95} from particle size distributions. It is also the first study to include measured IWC values greater than about 2 g m^{-3} and up to about 5 g m^{-3} .

Our results indicated that using a single power-law IWC– Z_{95} relationship allows for the radar retrieval of IWC with $\sim(10\%–30\%)$ bias and 40%–70% rms difference, depending on IWC. The IWC is also found to be underestimated by about 10%–20% for reflectivities lower than 15 dBZ, but is largely overestimated for reflectivities larger than 15 dBZ, which is attributed to non-Rayleigh scattering effects distorting the relationship between IWC and Z_{95} at large Z_{95} . A nonlinear relationship between $\log(\text{IWC})$ and Z_{95} has therefore been developed, which allows for IWC retrievals with biases less than 20% and rms differences of 20%–35% for $Z_{95} > 15 \text{ dBZ}$.

We then showed that the temperature variability of the IWC– Z_{95} relationship was large and that temperature could be used as an additional constraint to further reduce uncertainties on radar-derived IWCs, except when $Z > 16 \text{ dBZ}$ for temperatures lower than -25°C , where the nonlinear relationship between $\log(\text{IWC})$ and Z_{95} largely outperforms the temperature-dependent relationship. This variability with temperature has been clearly linked to and is consistent with the natural temperature variability of PSDs measured during the HAIC–HIWC campaign. Our variability study also shows that the nonlinear relationship (2) between $\log(\text{IWC})$ and Z_{95} should be used for convective profiles, and the temperature-dependent relationship (3) should be used for stratiform profiles to minimize IWC retrieval errors.

The radar results will be combined with those from a second just-completed flight program, and then examined for suitability in augmenting in situ IWC data collected for a future assessment of new aircraft certification rules for flight in ice crystals. Some preliminary results from the Darwin flight campaign related to these aviation objectives are reported upon here. Using all profiles collected during the field experiment (72 flight hours), a joint frequency distribution of radar-derived IWC and temperature within and around deep tropical convective cores was constructed. The results showed that IWC values greater than 4 g m^{-3} on $\sim 200\text{-m}$ -distance scales were exclusively found in convective profiles at all temperatures, and IWC values greater than 3 g m^{-3} were also almost exclusively found in convective profiles and at temperatures colder than -25°C . At the $-50^\circ \pm 5^\circ\text{C}$ level, which is the cruise level of many commercial jet aircraft, IWC values greater than 1.5 g m^{-3} were exclusively found in convective profiles during the HAIC–HIWC experiment. This result suggests that future efforts should be directed toward the development of a convective–stratiform index from geostationary satellites in order to detect and mitigate this type of high-IWC threat to civil aviation at this flight level. Nevertheless, it must be noted that recent analyses have highlighted that in-service engine events are most often associated with traverses across large convective anvils, suggesting that long exposures to moderate values of IWC may be as important as short exposures to high IWC. More studies will be needed to address this potentially different type of HIWC environment.

Acknowledgments. This research has received funding from the Federal Aviation Administration, Aviation Research Division, and Aviation Weather Division, under Agreement CON-I-2901 with the Australian Bureau of Meteorology. The research was also conducted as part of the European Union’s Seventh Framework Program in research, technological development, and demonstration under Grant Agreement ACP2-GA-2012-314314, and the European Aviation Safety Agency Research Program under Service Contract EASA.2013.FC27. Funding to support the development and testing of the isokinetic bulk TWC probe was provided by the FAA, NASA’s Aviation Safety Program, Environment and Climate Change Canada (formerly known as Environment Canada), and the National Research Council of Canada. Funding for the Darwin flight project was provided by the EU Seventh Framework Program agreement and the EASA contract noted above, the FAA, NASA’s Aviation Safety Program, the Boeing Company, Environment and Climate Change Canada, and Transport Canada.

REFERENCES

- Avery, M., D. Winker, A. J. Heymsfield, M. Vaughan, S. A. Young, Y. Hu, and C. Trepte, 2012: Cloud ice water content retrieved from the CALIOP space-based lidar. *Geophys. Res. Lett.*, **39**, L05808, doi:10.1029/2011GL050545.
- Baumgardner, D., and Coauthors, 2011: Airborne instruments to measure atmospheric aerosol particles, clouds and radiation: A cook's tour of mature and emerging technology. *Atmos. Res.*, **102**, 10–29, doi:10.1016/j.atmosres.2011.06.021.
- Bouniol, D., A. Protat, A. Plana-Fattori, M. Giraud, J.-P. Vinson, and N. Grand, 2008: Comparison of airborne and spaceborne 95-GHz radar reflectivity and evaluation of multiple scattering effects in spaceborne measurements. *J. Atmos. Oceanic Technol.*, **25**, 1983–1995, doi:10.1175/2008JTECHA1011.1.
- , and Coauthors, 2010: Using continuous ground-based radar and lidar measurements for evaluating the representation of clouds in four operational models. *J. Appl. Meteor. Climatol.*, **49**, 1971–1991, doi:10.1175/2010JAMC2333.1.
- Bringi, V. N., C. R. Williams, M. Thurai, and P. T. May, 2009: Using dual-polarized radar and dual-frequency profiler for DSD characterization: A case study from Darwin, Australia. *J. Atmos. Oceanic Technol.*, **26**, 2107–2122, doi:10.1175/2009JTECHA1258.1.
- Brown, P. R. A., and P. N. Francis, 1995: Improved measurements of the ice water content in cirrus using a total water probe. *J. Atmos. Oceanic Technol.*, **12**, 410–414, doi:10.1175/1520-0426(1995)012<0410:IMOTIW>2.0.CO;2.
- Cetrone, J., and R. A. Houze Jr., 2009: Anvil clouds of tropical mesoscale convective systems in monsoon regions. *Quart. J. Roy. Meteor. Soc.*, **135**, 305–317, doi:10.1002/qj.389.
- Chong, M., P. Amayenc, G. Scialom, and J. Testud, 1987: A tropical squall line observed during the COPT 81 experiment in West Africa. Part 1: Kinematic structure inferred from dual-Doppler radar data. *Mon. Wea. Rev.*, **115**, 670–694, doi:10.1175/1520-0493(1987)115<0670:ATSL0D>2.0.CO;2.
- Collis, S., A. Protat, P. T. May, and C. Williams, 2013: Statistics of storm updraft velocities from TWP-ICE including verification with profiling measurements. *J. Appl. Meteor. Climatol.*, **52**, 1909–1922, doi:10.1175/JAMC-D-12-0230.1.
- Davison, C. R., J. D. MacLeod, and J. W. Strapp, 2009: Naturally aspirating isokinetic total water content probe: Evaporator design and testing. *Proc. First AIAA Atmospheric and Space Environments Conf.*, San Antonio, TX, American Institute of Aeronautics and Astronautics, doi:10.2514/6.2009-3861.
- , J. W. Strapp, L. E. Lilie, T. P. Ratvasky, and C. Dumont, 2016: Isokinetic TWC evaporator probe: Calculations and system uncertainty analysis. *Proc. Eighth AIAA Atmospheric and Space Environments Conf.*, Washington, DC, American Institute of Aeronautics and Astronautics, doi:10.2514/6.2016-4060.
- Delanoë, J., and R. J. Hogan, 2010: Combined *CloudSat*-*CALIPSO*-*MODIS* retrievals of the properties of ice clouds. *J. Geophys. Res.*, **115**, D00H29, doi:10.1029/2009JD012346.
- , A. Protat, J. Testud, D. Bouniol, A. J. Heymsfield, A. Bansemmer, P. R. A. Brown, and R. M. Forbes, 2005: Statistical properties of the normalized ice particle size distribution. *J. Geophys. Res.*, **110**, D10201, doi:10.1029/2004JD005405.
- , R. J. Hogan, R. M. Forbes, A. Bodas-Salcedo, and T. H. M. Stein, 2011: Evaluation of ice cloud representation in the ECMWF and UK Met Office models using *CloudSat* and *CALIPSO* data. *Quart. J. Roy. Meteor. Soc.*, **137**, 2064–2078, doi:10.1002/qj.882.
- , A. Protat, O. Jourdan, J. Pelon, M. Papazzoni, R. Dupuy, J.-F. Gayet, and C. Jouan, 2013: Comparison of airborne in situ, airborne radar–lidar, and spaceborne radar–lidar retrievals of polar ice cloud properties sampled during the POLARCAT campaign. *J. Atmos. Oceanic Technol.*, **30**, 57–73, doi:10.1175/JTECH-D-11-00200.1.
- , A. Heymsfield, A. Protat, A. Bansemmer, and R. J. Hogan, 2014: Normalized particle size distribution for remote sensing application. *J. Geophys. Res. Atmos.*, **119**, 4204–4227, doi:10.1002/2013JD020700.
- Deng, M., G. Mace, Z. Wang, and R. P. Lawson, 2013: Evaluation of several A-Train ice cloud retrieval products with in situ measurements collected during the SPARTICUS campaign. *J. Appl. Meteor. Climatol.*, **52**, 1014–1030, doi:10.1175/JAMC-D-12-054.1.
- Dezitter, F., A. Grandin, J. L. Brenguier, F. Hervy, H. Schlager, P. Villedieu, and G. Zalamansky, 2013: HAIC—High altitude ice crystals. *Proc. Fifth AIAA Atmospheric and Space Environments Conf.*, San Diego, CA, American Institute of Aeronautics and Astronautics, doi:10.2514/6.2013-2674.
- EASA, 2011: Large aeroplane certification specifications in supercooled large drop, mixed phase, and ice crystal icing conditions. Notice of Proposed Amendment (NPA) 2011-03, European Aviation Safety Agency, 77 pp. [Available online at <http://easa.europa.eu/system/files/dfu/NPA%202011-03.pdf>.]
- Field, P. R., A. J. Heymsfield, and A. Bansemmer, 2006: Shattering and particle interarrival times measured by optical array probes in ice clouds. *J. Atmos. Oceanic Technol.*, **23**, 1357–1371, doi:10.1175/JTECH1922.1.
- Fontaine, E., A. Schwarzenboeck, J. Delanoë, W. Wobrock, D. Leroy, R. Dupuy, C. Gourbeyre, and A. Protat, 2014: Constraining mass-diameter relations from hydrometeor images and cloud radar reflectivities in tropical and oceanic convection. *Atmos. Chem. Phys.*, **14**, 11367–11392, doi:10.5194/acp-14-11367-2014.
- Gamache, J. F., and R. A. Houze Jr., 1982: Mesoscale air motions associated with a tropical squall line. *Mon. Wea. Rev.*, **110**, 118–135, doi:10.1175/1520-0493(1982)110<0118:MAMA WA>2.0.CO;2.
- Giangrande, S. E., S. Collis, J. Straka, A. Protat, C. Williams, and S. Krueger, 2013: A summary of convective-core vertical velocity properties using ARM UHF wind profilers in Oklahoma. *J. Appl. Meteor. Climatol.*, **52**, 2278–2295, doi:10.1175/JAMC-D-12-0185.1.
- Government Printing Office, 2010: Federal Aviation Administration Notice of Proposed Rulemaking: Airplane and engine certification requirements in supercooled large drop, mixed phase, and ice crystal icing conditions. *Federal Register*, Vol. 75, No. 124, 37 311–37 339. [Available online at <http://edocket.access.gpo.gov/2010/pdf/2010-15726.pdf>.]
- Grandin, A., J.-M. Merle, M. Weber, J. W. Strapp, A. Protat, and P. King, 2014: AIRBUS flight tests in high ice water content regions. *Proc. Sixth AIAA Atmospheric and Space Environments Conf.*, Atlanta, GA, American Institute of Aeronautics and Astronautics, doi:10.2514/6.2014-2753.
- Grzych, M., and J. Mason, 2010: Weather conditions associated with jet engine power loss and damage due to ingestion of ice particles: What we've learned through 2009. Preprints, *14th Conf. on Aviation, Range, and Aerospace Meteorology*, Atlanta, GA, Amer. Meteor. Soc., 6.8. [Available online at https://ams.confex.com/ams/90annual/techprogram/paper_165923.htm.]

- Hallett, J., and S. C. Mossop, 1974: Production of secondary ice particles during the riming process. *Nature*, **249**, 26–28, doi:10.1038/249026a0.
- Heymsfield, A. J., 2007: On measurements of small ice particles in clouds. *Geophys. Res. Lett.*, **34**, L23812, doi:10.1029/2007GL030951.
- , C. Schmitt, A. Bansemer, and C. H. Twohy, 2010: Improved representation of ice particle masses based on observations in natural clouds. *J. Atmos. Sci.*, **67**, 3303–3318, doi:10.1175/2010JAS3507.1.
- , —, and —, 2013: Ice cloud particle size distributions and pressure-dependent terminal velocities from in situ observations at temperatures from 0° to –86°C. *J. Atmos. Sci.*, **70**, 4123–4154, doi:10.1175/JAS-D-12-0124.1.
- Heymsfield, G. M., L. Tian, A. J. Heymsfield, L. Li, and S. Guimond, 2010: Characteristics of deep tropical and subtropical convection from nadir-viewing high-altitude airborne Doppler radar. *J. Atmos. Sci.*, **67**, 285–308, doi:10.1175/2009JAS3132.1.
- Hogan, R. J., M. P. Mittermaier, and A. J. Illingworth, 2006: The retrieval of ice water content from radar reflectivity factor and temperature and its use in evaluating a mesoscale model. *J. Appl. Meteor. Climatol.*, **45**, 301–317, doi:10.1175/JAM2340.1.
- Illingworth, A. J., and Coauthors, 2007: Cloudnet: Continuous evaluation of cloud profiles in seven operational models using ground-based observations. *Bull. Amer. Meteor. Soc.*, **88**, 883–898, doi:10.1175/BAMS-88-6-883.
- Jackson, R. C., G. M. McFarquhar, J. Stith, M. Beals, R. A. Shaw, J. Jensen, J. Fugal, and A. Korolev, 2014: An assessment of the impact of antishattering tips and artifact removal techniques on cloud ice size distributions measured by the 2D cloud probe. *J. Atmos. Oceanic Technol.*, **31**, 2567–2590, doi:10.1175/JTECH-D-13-00239.1.
- Jensen, E., D. Starr, and O. B. Toon, 2004: Mission investigates tropical cirrus clouds. *Eos, Trans. Amer. Geophys. Union*, **85**, 45–50, doi:10.1029/2004EO050002.
- Korolev, A., and G. A. Isaac, 2005: Shattering during sampling by OAPs and HVPS. Part I: Snow particles. *J. Atmos. Oceanic Technol.*, **22**, 528–542, doi:10.1175/JTECH1720.1.
- Lawson, R. P., L. J. Angus, and A. J. Heymsfield, 1998: Cloud particle measurements in thunderstorm anvils and possible threat to aviation. *J. Aircr.*, **35**, 113–121, doi:10.2514/2.2268.
- , D. O'Connor, P. Zmarzly, K. Weaver, B. Baker, Q. Mo, and H. Jonsson, 2006: The 2D-S (stereo) probe: Design and preliminary tests of a new airborne, high-speed, high-resolution particle imaging probe. *J. Atmos. Oceanic Technol.*, **23**, 1462–1477, doi:10.1175/JTECH1927.1.
- Li, J.-L. F., and Coauthors, 2012: An observationally based evaluation of cloud ice water in CMIP3 and CMIP5 GCMs and contemporary reanalyses using contemporary satellite data. *J. Geophys. Res.*, **117**, D16105, doi:10.1029/2012JD017640.
- Li, L., G. M. Heymsfield, L. Tian, and P. E. Racette, 2005: Measurements of ocean surface backscattering using an airborne 95-GHz cloud radar—Implication for calibration of airborne and spaceborne W-band radars. *J. Atmos. Oceanic Technol.*, **22**, 1033–1045, doi:10.1175/JTECH1722.1.
- Mace, G. G., 2010: Cloud properties and radiative forcing over the maritime storm tracks of the North Atlantic and Southern Ocean as derived from A-Train. *J. Geophys. Res.*, **115**, D10201, doi:10.1029/2009JD012517.
- Mason, J. G., J. W. Strapp, and P. Chow, 2006: The ice particle threat to engines in flight. *Proc. 44th AIAA Aerospace Sciences Meeting*, Reno, NV, American Institute of Aeronautics and Astronautics, doi:10.2514/6.2006-206.
- Matrosov, S. Y., and A. J. Heymsfield, 2008: Estimating ice content and extinction in precipitating cloud systems from *CloudSat* radar measurements. *J. Geophys. Res.*, **113**, D00A05, doi:10.1029/2007JD009633.
- , A. V. Korolev, and A. J. Heymsfield, 2002: Profiling cloud ice mass and particle characteristic size from Doppler radar measurements. *J. Atmos. Oceanic Technol.*, **19**, 1003–1018, doi:10.1175/1520-0426(2002)019<1003:PCIMAP>2.0.CO;2.
- May, P. T., and D. K. Rajopadhyaya, 1999: Vertical velocity characteristics of deep convection over Darwin, Australia. *Mon. Wea. Rev.*, **127**, 1056–1071, doi:10.1175/1520-0493(1999)127<1056:VVCODC>2.0.CO;2.
- , A. R. Jameson, T. D. Keenan, P. E. Johnston, and C. Lucas, 2002: Combined wind profiler/polarimetric radar studies of the vertical motion and microphysical characteristics of tropical sea-breeze thunderstorms. *Mon. Wea. Rev.*, **130**, 2228–2239, doi:10.1175/1520-0493(2002)130<2228:CWPPRS>2.0.CO;2.
- Mishchenko, M. I., L. D. Travis, and D. W. Mackowski, 1996: T-matrix computations of light scattering by nonspherical particles: A review. *J. Quant. Spectrosc. Radiat. Transfer*, **55**, 535–575, doi:10.1016/0022-4073(96)00002-7.
- Nishi, N., M. K. Yamamoto, T. Shimomai, A. Hamada, and S. Fukao, 2007: Fine structure of vertical motion in the stratiform precipitation region observed by a VHF Doppler radar installed in Sumatra, Indonesia. *J. Appl. Meteor. Climatol.*, **46**, 522–537, doi:10.1175/JAM2480.1.
- Oguchi, T., 1983: Electromagnetic wave propagation and scattering in rain and other hydrometeors. *Proc. IEEE*, **71**, 1029–1078, doi:10.1109/PROC.1983.12724.
- Penide, G., V. Kumar, A. Protat, and P. T. May, 2013a: Statistics of drop size distribution parameters and rain rates for stratiform and convective precipitation during the north Australian wet season. *Mon. Wea. Rev.*, **141**, 3222–3237, doi:10.1175/MWR-D-12-00262.1.
- , A. Protat, V. Kumar, and P. T. May, 2013b: Comparison of two convective/stratiform precipitation classification techniques: Horizontal reflectivity texture versus drop size distribution-based approach. *J. Atmos. Oceanic Technol.*, **30**, 2788–2797, doi:10.1175/JTECH-D-13-00019.1.
- Protat, A., and I. Zawadzki, 1999: A variational method for real-time retrieval of three-dimensional wind field from multiple-Doppler bistatic radar network data. *J. Atmos. Oceanic Technol.*, **16**, 432–449, doi:10.1175/1520-0426(1999)016<0432:AVMFRT>2.0.CO;2.
- , and C. R. Williams, 2011: The accuracy of radar estimates of ice terminal fall speed from vertically pointing Doppler radar measurements. *J. Appl. Meteor. Climatol.*, **50**, 2120–2138, doi:10.1175/JAMC-D-10-05031.1.
- , and Coauthors, 2004: Le projet RALI: Combinaison d'un radar nuage et d'un lidar pour l'étude des nuages faiblement précipitants (A combination of cloud radar and lidar for the study of precipitating low clouds). *Météorologie*, **47**, 23–33, doi:10.4267/2042/36076.
- , J. Delanoë, D. Bouniol, A. J. Heymsfield, A. Bansemer, and P. Brown, 2007: Evaluation of ice water content retrievals from cloud radar reflectivity and temperature using a large airborne in situ microphysical database. *J. Appl. Meteor. Climatol.*, **46**, 557–572, doi:10.1175/JAM2488.1.
- , and Coauthors, 2009: Assessment of *CloudSat* reflectivity measurements and ice cloud properties using ground-based and airborne cloud radar observations. *J. Atmos. Oceanic Technol.*, **26**, 1717–1741, doi:10.1175/2009JTECHA1246.1.

- , J. Delanoë, E. O'Connor, and T. L'Ecuyer, 2010a: The evaluation of *CloudSat*-derived ice microphysical products using ground-based cloud radar and lidar observations. *J. Atmos. Oceanic Technol.*, **27**, 793–810, doi:[10.1175/2009JTECHA1397.1](https://doi.org/10.1175/2009JTECHA1397.1).
- , —, A. Plana-Fattori, P. T. May, and E. O'Connor, 2010b: The statistical properties of tropical ice clouds generated by the West African and Australian monsoons from ground-based radar–lidar observations. *Quart. J. Roy. Meteor. Soc.*, **136** (S1), 345–363, doi:[10.1002/qj.490](https://doi.org/10.1002/qj.490).
- , —, P. T. May, J. Haynes, C. Jakob, E. O'Connor, M. Pope, and M. Wheeler, 2011: The variability of tropical ice cloud properties as a function of the large-scale context from ground-based radar–lidar observations over Darwin, Australia. *Atmos. Chem. Phys.*, **11**, 8363–8384, doi:[10.5194/acp-11-8363-2011](https://doi.org/10.5194/acp-11-8363-2011).
- Steiner, M., R. A. Houze Jr., and S. E. Yuter, 1995: Climatological characterization of three-dimensional storm structure from operational radar and rain gauge data. *J. Appl. Meteor.*, **34**, 1978–2007, doi:[10.1175/1520-0450\(1995\)034<1978:CCOTDS>2.0.CO;2](https://doi.org/10.1175/1520-0450(1995)034<1978:CCOTDS>2.0.CO;2).
- Stephens, G. L., S.-C. Tsay, P. W. Stackhouse, and P. J. Flatau, 1990: The relevance of the microphysical and radiative properties of cirrus clouds to climate and climatic feedback. *J. Atmos. Sci.*, **47**, 1742–1754, doi:[10.1175/1520-0469\(1990\)047<1742:TROTMA>2.0.CO;2](https://doi.org/10.1175/1520-0469(1990)047<1742:TROTMA>2.0.CO;2).
- Strapp, J. W., and Coauthors, 2016a: The High Ice Water Content (HIWC) study of deep convective clouds: Science and technical plan. FAA Rep. DOT/FAA/TC-14/31, in press.
- , L. E. Lilie, T. P. Ratvasky, C. R. Davison, and C. Dumont, 2016b: Isokinetic TWC evaporator probe: Development of the IKP2 and performance testing for the HAIC-HIWC Darwin 2014 and Cayenne-2015 field campaigns. *Proc. Eighth AIAA Atmospheric and Space Environments Conf.*, Washington, DC, American Institute of Aeronautics and Astronautics, paper 2016–4059, doi:[org/10.2514/6.2016-4059](https://doi.org/10.2514/6.2016-4059).
- Su, H., J. H. Jiang, D. G. Vane, and G. L. Stephens, 2008: Observed vertical structure of tropical oceanic clouds sorted in large-scale regimes. *Geophys. Res. Lett.*, **35**, L24704, doi:[10.1029/2008GL035888](https://doi.org/10.1029/2008GL035888).
- Thurai, M., V. N. Bringi, and P. T. May, 2010: CPOL radar-derived drop size distribution statistics of stratiform and convective rain for two regimes in Darwin, Australia. *J. Atmos. Oceanic Technol.*, **27**, 932–942, doi:[10.1175/2010JTECHA1349.1](https://doi.org/10.1175/2010JTECHA1349.1).
- Toon, O. B., and Coauthors, 2010: Planning, implementation, and first results of the Tropical Composition, Cloud and Climate Coupling Experiment (TC4). *J. Geophys. Res.*, **115**, D00J04, doi:[10.1029/2009JD013073](https://doi.org/10.1029/2009JD013073).
- Waliser, D. E., and Coauthors, 2009: Cloud ice: A climate model challenge with signs and expectations of progress. *J. Geophys. Res.*, **114**, D00A21, doi:[10.1029/2008JD010015](https://doi.org/10.1029/2008JD010015).
- Zipser, E. J., and Coauthors, 2009: The Saharan air layer and the fate of African easterly waves: NASA's AMMA field study of tropical cyclogenesis. *Bull. Amer. Meteor. Soc.*, **90**, 1137–1156, doi:[10.1175/2009BAMS2728.1](https://doi.org/10.1175/2009BAMS2728.1).